Acta Materialia 312 (2026) 122232

Contents lists available at ScienceDirect

Acta Materialia

journal homepage: www.elsevier.com/locate/actamat

Full length article

Inter-zone synergetic strengthening and ductilization in an optimized dual-phase heterostructure via dispersed micro-shear bands

Bo Gao [a], Xinxin Dong [a], Lirong Xiao [b], Yi Liu [c], Dongdi Yin [d,*], Hao Zhou [a,*], Yuntian Zhu [a,e,*]

[a] Department of Heterostructured Materials, Interdisciplinary Research Center, Liaoning Academy of Materials, Shenyang, 110167, China
[b] Nano and Heterogeneous Materials Center, School of Materials Science and Engineering, Nanjing University of Science and Technology, Nanjing, 210094, China
[c] School of Mechanical Engineering, Tongling University, Tongling, 244061, China
[d] Key Laboratory of Advanced Technologies of Materials, Ministry of Education, School of Materials Science and Engineering, Southwest Jiaotong University, Chengdu, 610031, China
[e] Department of Materials Science and Engineering, City University of Hong Kong, Hong Kong, 999077, China

ARTICLE INFO

Keywords:
Heterostructured materials
Dual-phase structure
Strain/stress partitioning
Micro shear bands
Inter-zone synergetic effects

ABSTRACT

Heterostructured materials (HSMs) offer a promising path to overcome the strength-ductility trade-off for the notable synergetic strengthening and hardening effects. The zone configurations of HSMs play an important role in maximizing the inter-zone synergetic effects. In this work, the ferritic and martensitic zones in low-carbon steel were tailored by adjusting rolling pre-strains and subsequent intercritical annealing durations. A larger rolling pre-strain (80% reduction) and a longer annealing duration (t = 15 min) facilitate the formation of an optimized dual-phase heterostructure, with the equiaxed ferrite grains dispersedly distributed in the ultrafine-grained martensite matrix. This dispersed heterostructured dual-phase steel (HSDP3) achieves an ultrahigh strength of 2.0 GPa while retaining considerable ductility, with a markedly enhanced strain-hardening rate compared to the lower-strain HSDP steels (HSDP1 and HSDP2). The improved mechanical properties are contributed by the favorable inter-zone synergetic effects mediated by dispersed micro-shear bands (SBs). Specifically, the dispersed micro-SBs results in a developed hierarchical plastic deformation within heterogenous zones, including deformed ferrite, severely deformed martensite and slightly deformed martensite. The slightly deformed martensite significantly contributes to the strain partitioning with ferrite, thus promoting hetero-deformation induced (HDI) hardening especially at the low-strain stage. Additionally, the dense stable SBs force more martensite to accommodate severe strain together with ferrite, improving strain hardening and ductility at large-strain stage.

1. Introduction

High-strength metallic structural materials with exceptional ductility are indispensable for industrial applications, particularly in ensuring lightweight transportation and infrastructure safety [1]. However, the inherent trade-off between strength and ductility persists as a fundamental challenge in metallic materials, primarily due to the exhaustion of strain hardening capability at elevated strength levels [2]. Extensive tunability of the microstructural characteristics and corresponding mechanical properties has been achieved through multi-element alloying strategies [3,4]. However, such compositionally complex approaches conflict with sustainability principles in metallic materials development. This contradiction necessitates innovative design paradigms to mitigate critical element dependence while maintaining property benchmarks. Recently, heterostructured materials (HSMs) have emerged as a promising solution to alleviate strength-ductility trade-off by activating extra strengthening and hardening mechanisms [5–7].

The exceptional mechanical performance of HSMs arises from strategically designed hetero-zones with contrasting mechanical/physical properties [8], as evidenced in heterogeneous lamellar structured Ti [9,10], laminate structured Cu/Cu-Zn [11,12], harmonic structured Cu [13], gradient structured Ni [14], etc. The prominent inter-zone constraint during deformation changes the zone-scale stress/strain status, especially in the regions near zone boundaries. Deformation

* Corresponding authors.
E-mail addresses: ahnydd@swjtu.edu.cn (D. Yin), hzhou@lam.ln.cn (H. Zhou), y.zhu@cityu.edu.hk (Y. Zhu).

https://doi.org/10.1016/j.actamat.2026.122232
Received 4 January 2026; Received in revised form 10 April 2026; Accepted 13 April 2026
Available online 14 April 2026

incompatibility between constituent zones promotes strain partitioning and geometrically necessary dislocations (GNDs) accumulation near zone boundaries, generating long-range hetero-deformation induced (HDI) stress to provide additional strengthening and hardening [15,16]. Concurrently, the inherent zone contrast mediates a unique synergetic deformation behavior of stable dispersed micro shear bands (SBs) in HSMs [17–19]. Shear instability tends to occur in the hard zones of HSMs due to their limited strain hardening capacity. The constraint of soft zones helps with arresting the propagation of catastrophic shear instability in hard zones, and forming dispersed stable micro-SBs [17]. This effectively prevents strain localization and macroscopic shear instability, thus sustaining high ductility. These synergistic effects make heterostructural architecture compelling for enhancing strength-ductility synergy.

Recent insights highlight the critical dependence of these inter-zone synergistic effects on the configurations of heterogeneous zones. First, the soft-zone volume fraction (V_{soft}) fundamentally dictates the effectiveness of the constraint [20]. For instance, configurations with soft zones embedded in a hard matrix ($V_{soft}<$ 50%) demonstrates superior synergistic mechanical effects compared to the inverse configuration [21,22]. Second, the hetero boundary affected regions (Hbar) emerges as a governing microstructural feature where its volume fraction (V_{Hbar}) and synergistic hardening efficiency ($K_{hardening}$) jointly determine extra work hardening capacity of heterostructures [20]. Optimized Hbar requires to tune the zone configurations: increasing the density of zone interfaces through uniform soft zone dispersion in hard matrix to renders greater extra hardening effects [23]; enhancing inter-zone mechanical incompatibility between hetero-zones to intensify plastic strain gradient within Hbar. These findings established the zone volume fraction, zone distribution, and inter-zone mechanical incompatibility as key controls for engineering the inter-zone synergetic effects.

Meanwhile, it is imperative to discern the feedback of HDI stress and micro-SBs on the deformation behaviors of heterogeneous zones to effectively tailor these synergetic effects for optimized properties. Extensive researches have elucidated the role of HDI stress in evoking unusual microstructural responses within hetero-zones. It facilitates critical phase transformation, twinning, cross-slip of extended dislocations in soft zones [15,24,25], which is difficult to be activated in their homogeneous counterparts, thus producing extra work hardening. In addition, the dynamically reinforced HDI stress has been reported to cause the strength reversal between hard and soft zones in hetero-structured duplex stainless steel. This allows hetero-zones to alternately bear strain, thereby preventing premature damage localization in the initially soft zones [26]. While the role of HDI stress in promoting hetero-zone interactions and enhancing mechanical properties is increasingly well-understood, the underlying synergetic strengthening and ductilization mechanisms mediated by micro-SBs remain unclear. Fundamental issues have emerged from recent developments: the role of micro-SBs in mediating deformation behavior across heterogeneous zones, particularly within hard zones; the influence of soft zones configuration on formation and propagation of micro-SBs; strategic design principles for maximizing inter-zone synergistic effects through tailored heterostructure architectures.

This study employs the widely studied dual-phase heterostructure as a model system, specifically a ferrite-martensite (F-M) dual-phase structure was tailored in low-carbon steel through controlled initial plastic deformation and subsequent annealing [27–29]. This work focuses on evoking the inter-zone synergetic effects for enhanced strength-ductility synergy by tuning phase configurations (e.g., volume fraction, distribution, strength difference), as well as to elucidating the effects of dual-phase configurations on micro-SBs formation and their feedback on deformation behaviors of heterogeneous zones. Systematical experiments and modeling results demonstrate that the mechanical properties can be improved in an optimized dual-phase heterostructure through the inter-zone synergetic effects driven by dispersed micro-SBs. The formation, stabilization, and contribution of the dispersed micro-SBs are explored in depth. This work will shed light on utilizing the inter-zone synergetic strengthening and ductilization effects mediated by dispersed micro-SBs in HSMs to achieve optimized mechanical properties.

2. Materials and methods

2.1. Material and processing route

A low-carbon and low-alloy steel with the chemical composition of Fe-0.24C-0.31Si-0.94Mn-0.84Cr-1.18Ni-0.31%Mo (wt.%) was used in this work. Fig. S1a shows the schematic diagram of the thermo-mechanical processing route. Three sequential steps were designed to generate and subsequently tune dual-phase microstructures. First, the as-received 8-mm-thick steel plate was austenitized at 900 °C for 1 h and water quenched to room temperature, followed by intercritical annealing (IA) at 760 °C for 10 min to obtain the dual-phase steel (hereafter 760DP). Second, the 760DP steel was warm rolled at 300 °C with thickness reductions of 30% and 80%. They correspond to the equivalent true strains (ε) of 0.41 and 1.86, respectively, according to Ref [30]

$$\varepsilon = -\frac{2}{\sqrt{3}} ln\left(\frac{t_f}{t_0}\right) \tag{1}$$

where t_f and t_0 are the final and initial thickness. Finally, a second IA treatment was carried out on the deformed steels at 760 °C for 3–15 min to systematically tailor the DP heterostructure. As indicated by the JMatPro-calculated phase fraction diagram (Fig. S1b), the equilibrium austenite fraction at 760 °C is ~83%, providing a wide processing window for tuning phase fractions via controlled IA durations.

2.2. Tests of mechanical properties

Dog-bone shaped tensile specimens with a gauge length of 10 mm and a width of 2.5 mm were cut from the steel plates, with their longitudinal axes aligned parallel to the rolling direction. All the tensile specimens were polished to a mirror finish before tensile tests. Quasi-static uniaxial tensile tests were performed using an LTM-20KN testing machine at a strain rate of 5×10^{-4} s^{-1} at room temperature. To estimate the Bauschinger effect, cyclic load-unload-reload (LUR) tensile tests were performed. In each LUR cycle, the specimen was strained to an assigned level, unloaded to 100 N, and subsequently reloaded. The emergence of mechanical hysteresis loops was taken as evidence of GND-based hetero-deformation. The HDI stress was calculated based on Eq. (2) [27,31].

$$\sigma_{HDI} = (\sigma_u + \sigma_r)/2 \tag{2}$$

where σ_u and σ_r are unloading and reloading yield stresses, respectively, both of which were obtained from the corresponding hysteresis loops in each unload-reload cycle.

2.3. Microstructural characterization

Cross-section samples were ground, polished and etched with a 2% Nital solution. Microstructures were observed by a scanning electron microscopy (SEM, FEI Quanta 250F), and the volume fraction of martensite was quantified using the Image J software [32]. Electron backscattering diffraction (EBSD) tests were conducted on a Zeiss Auriga focused ion beam-SEM to investigate the microstructure, using a scanning step size of 50 nm and an accelerating voltage of 15 kV. Especially, the GND density distribution was extracted based on the kernel average misorientation (KAM) in EBSD results using the commercial AZtecCrystal software (Oxford Instruments plc). Substructures within DP steels were further revealed by transmission electron microscope (TEM, FEI Titan G6 60–300) operated at 300 kV. TEM foils were sectioned from

the steel plate, mechanically tinned to ~20 μm, and subsequently perforated by ion milling (Gatan PIPS II 695) at −30 °C.

2.4. Strain distribution analysis

To investigate the synergetic deformation in the DP heterostructure, *in-situ* tensile tests were conducted inside an SEM using a commercial micro-tensile tester (MINI-MTS2000, Qiyue Technology Co., Ltd, China), as shown in Fig. S1c. The cross-section surface of each dog-bone shaped specimen was grinded, polished, and etched to visualize the microstructure before tensile testing. SEM images of the region of interest (ROI) in gauge section were captured at successive tensile strains. The intrinsic fine contrast in the etched microstructure of DP steels was directly served as the natural speckle pattern for DIC calculation, consistent with earlier studies [33,34]. In order to simplify the complex strain components into a single uniaxial strain value to facilitate analysis, the von Mises equivalent strain is used to assess the strain evolution [34,35]. The relationship between the von Mises equivalent strain and tensile strain components is detailed in the supplementary material. In this work, the spatial distribution of these strain components and the resultant von Mises equivalent strain within the DP heterostructure were quantified using ARAMIS software (GOM GmbH).

3. Results

3.1. Microstructural evolution

Fig. 1 shows the progressive microstructural refinement induced by warm rolling. The as-received 760DP steel (Fig. 1a) exhibits a fibrous dual-phase morphology with a martensite volume fraction (V_M) of 52%, and ferrite containing a high density of carbides. Moderate rolling at 30% reduction initiates morphological alignment along the rolling direction (Fig. 1b1), but retains coarse martensite domains (>2 μm) due to incomplete grain refinement. In contrast, high-strain deformation at 80% reduction results in pronounced refinement of both martensite and ferrite (Fig. 1b2). TEM characterization (Fig. 1c-e) further quantifies this refinement pathway. In the undeformed 760DP state, ferrite and martensite can be distinguished by contrast (Fig. 1c). The fibrous ferrite with a width (d_F) of ~1 μm is separated into several sub-cells by dislocations formed during the martensitic transformation, while the adjacent fibrous martensite is divided into several fine lath with an average width (d_{Lath}) of ~300 nm. After 30% rolling reduction, these features evolve into a lamellar structure with reduced lamellar size (d_L) of ~200 nm and elevated dislocation densities (Fig. 1d1 and d2). As shown in Fig. 1e1 and e2, severe deformation of 80% reduction drives extreme microstructural refinement into nano-lamellar architecture bounded by high-angle boundaries (HABs), as evidenced by the pronounced misorientation between the adjacent lamellae [36]. Quantitative analysis (Fig. 1f) demonstrates that the average lamellar thickness decreases

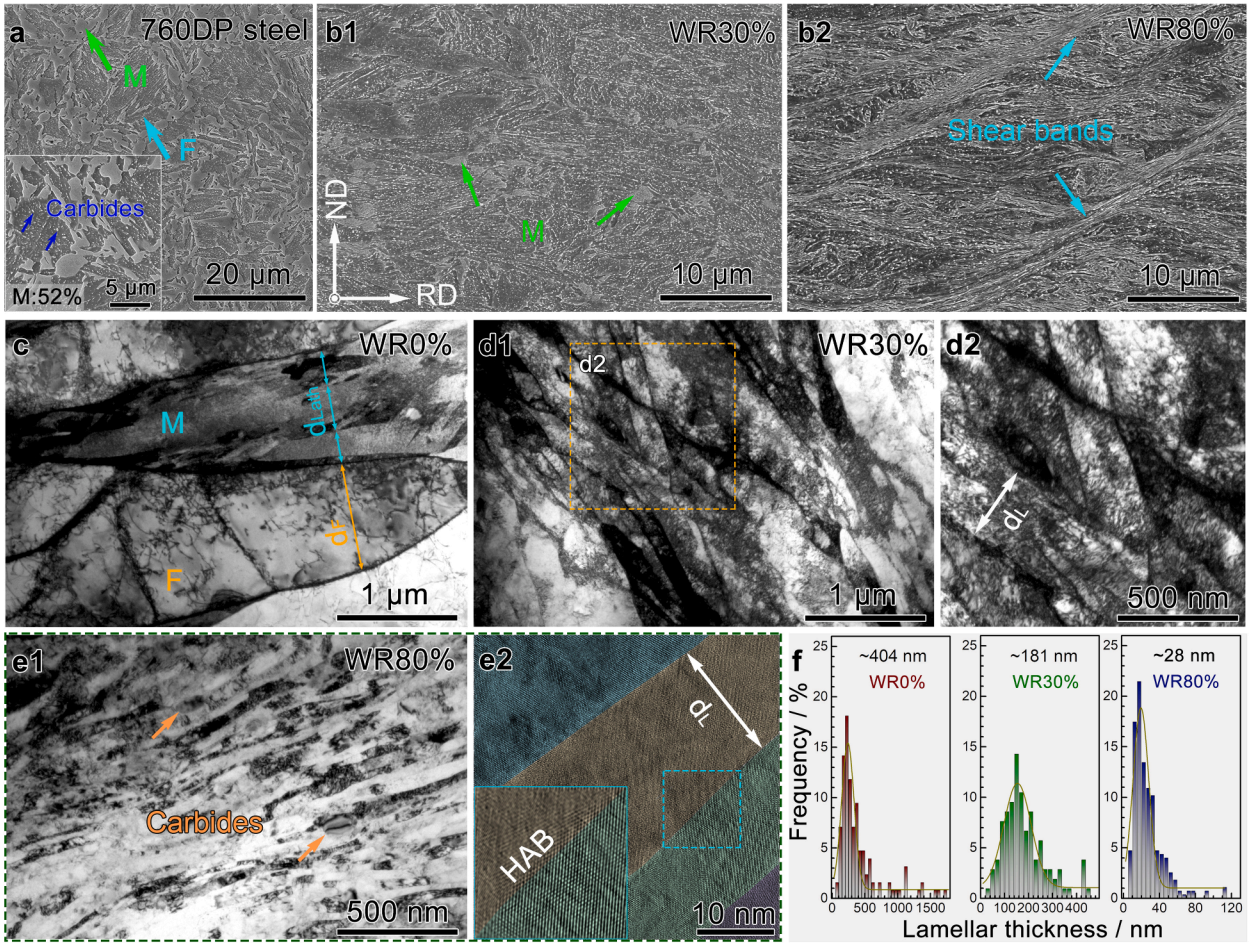

Fig. 1. Microstructural evolution of 760DP steel during warm rolling. (a) dual-phase microstructure produced by intercritical annealing at 760 °C, (b1) and (b2) SEM micrographs of 760DP steel rolled with 30% and 80% thickness reductions, respectively, (c) TEM micrograph of the undeformed 760DP steel (WR0%), (d1) and (d2) TEM micrographs of 760DP steel after 30% rolling reduction, (e1) TEM micrographs of 760DP steel after 80% rolling reduction, (e2) HRTEM image showing distinct nano-lamellae indicated by different colors, (f) lamellar thickness distributions of steels processed at different rolling reductions.

markedly from 404 to 181 and ultimately to 28 nm with increasing rolling strain.

Intercritical annealing at 760 °C for different durations was employed to tune the dual-phase configurations of the rolled steels, with microstructures shown in Fig. 2a-c and the corresponding evolution of V_M summarized in Fig. 2d In the undeformed (0%) condition, annealing for 3 min produces a microstructure comprising ferrite, carbides, and isolated martensite islands (~35%), exhibiting the limited extent of austenite formation during the short annealing period [37]. Extending the annealing time to 5 min and 15 min increases V_M to 49% and 71%, respectively, gradually constructing typical DP morphology. Rolling strain markedly accelerates austenite formation and transformation kinetics. At identical annealing times, the 30% rolled samples achieve V_M of 52%, 65%, and 80%, while the 80% rolled specimens reach 57%, 70%, and 82%. The rise in V_M is accompanied by several microstructural consequences. First, higher V_M leads to complete carbide dissolution, producing a full DP structure. Second, refinement of ferrite grains is enhanced; for instance, in the 80% rolled samples, ferrite grain size (D_F) decreases from 1.45 μm to 1.13 μm and 1.02 μm with increasing V_M (Fig. 2e). Third, the ferrite spatial distribution transitions from clustered regions to a more homogeneous dispersion as V_M increases.

A larger initial rolling pre-strain not only results in higher V_M but also influences the martensitic grain refinement. EBSD band-contrast maps (Fig. 3a–c) show that prior austenite grains (PAGs) decompose into packets and blocks separated by high-angle boundaries (HABs, θ>15°), consistent with Kurdjumov-Sachs orientation relationships [38, 39]. These HABs, corresponding to block and packet boundaries, serve as effective barriers to dislocation motion and thus play a central role in governing the yield strength [40]. Therefore, the effective grain size of martensite (D_M) was estimated following Ref [41] by measuring the linear spacing between the HABs (Fig. 3d1 and d2). Under identical heat-treatment condition (760 °C, 15 min), increasing the initial rolling pre-strain progressively refines D_M from 0.61 μm to 0.58 μm and ultimately to 0.42 μm (Fig. 3e).

As described above, the volume fraction, grain size, and spatial distribution of the DP heterostructure have been effectively tailored by adjusting the initial rolling strain and subsequent intercritical annealing duration. A larger rolling pre-strain (80% reduction, ε=1.86) and a longer annealing duration (t = 15 min) facilitate the formation of a dispersed heterostructured dual-phase (HSDP) steel, where soft ferrite grains are embedded in a continuous hard martensitic matrix. Under these processing conditions, the elevated carbon content, increased dislocation density, and refined grain size collectively make the martensite much stronger than ferrite phase. The pronounced strength mismatch introduces a considerable mechanical incompatibility between the two phases.

3.2. Tensile properties

Fig. 4a1 to a3 show the engineering stress-strain curves, with corresponding mechanical properties summarized in Table 1. Before intercritical annealing, increasing the imposed warm-rolling (WR) strain leads to a pronounced strengthening effect: the yield strength (YS) increases from 643 MPa to 1192 MPa and ultimately 1950 MPa, accompanied by increases in ultimate tensile strength (UTS) from 987 to 1304 and 2021 MPa. The as-rolled nanostructured samples (WR30% and WR80%), however, exhibit very limited ductility (~2%) due to their high density of deformation-induced lattice defects. IA treatment substantially modifies this strength-ductility balance. Uniform elongation (UE) and elongation to fracture (ETF) improve markedly relative to the as-rolled state then gradually decline as annealing time is extended. Inevitably, both YS and UTS decrease immediately after annealing due to the significant recovery and recrystallization at high temperature, however, they progressively increase with extended annealing. After 15 min of IA, the tensile strength of the three DP steels, subjected to 0%, 30%, and 80% rolling pre-strain, equal or even exceed those of their as-rolled counterparts. These three representative heterostructured DP steels are hereafter termed as HSDP1, HSDP2, and HSDP3, respectively.

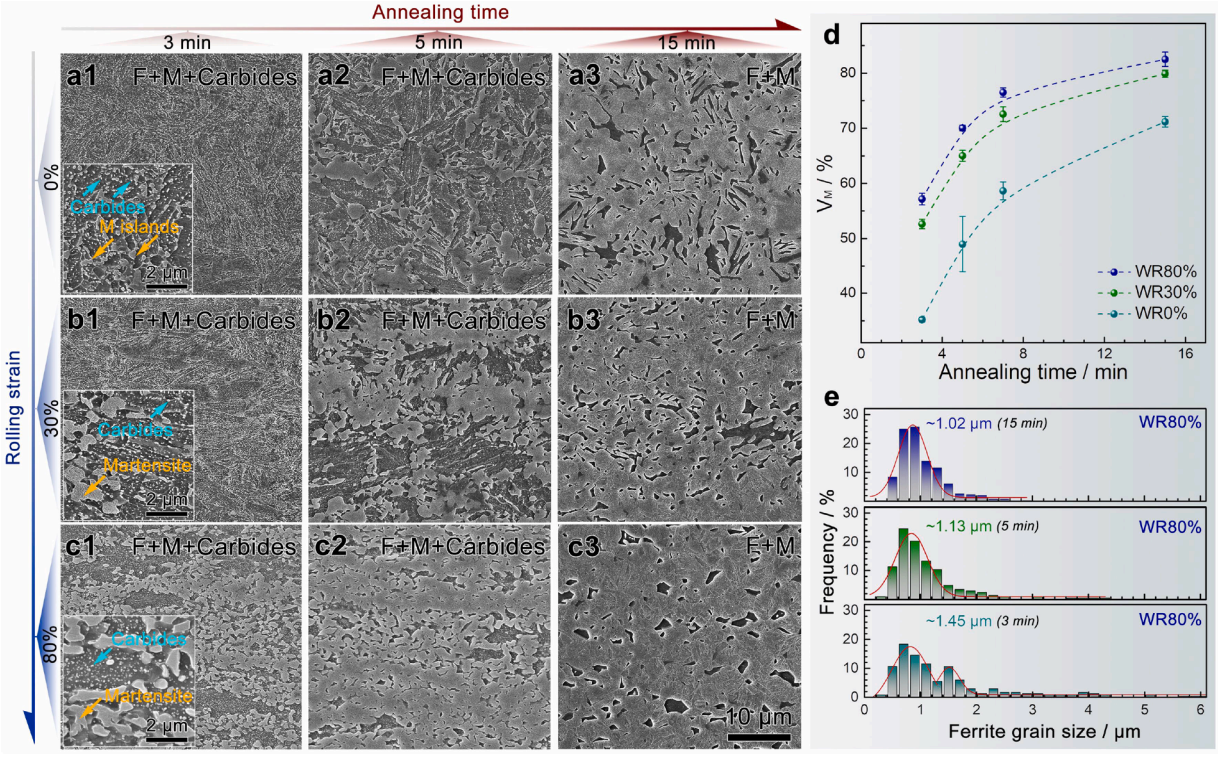

Fig. 2. Representative SEM micrographs of steels subjected to different initial rolling pre-strains and annealing durations at 760 °C. (a1)–(a3) 0% rolled, (b1)–(b3) 30% rolled, (c1)–(c3) 80% rolled, shown after 3, 5, and 15 min, respectively, (d) evolution of V_M with annealing time, (e) distribution of D_F for the 80% rolled steels annealed for different times.

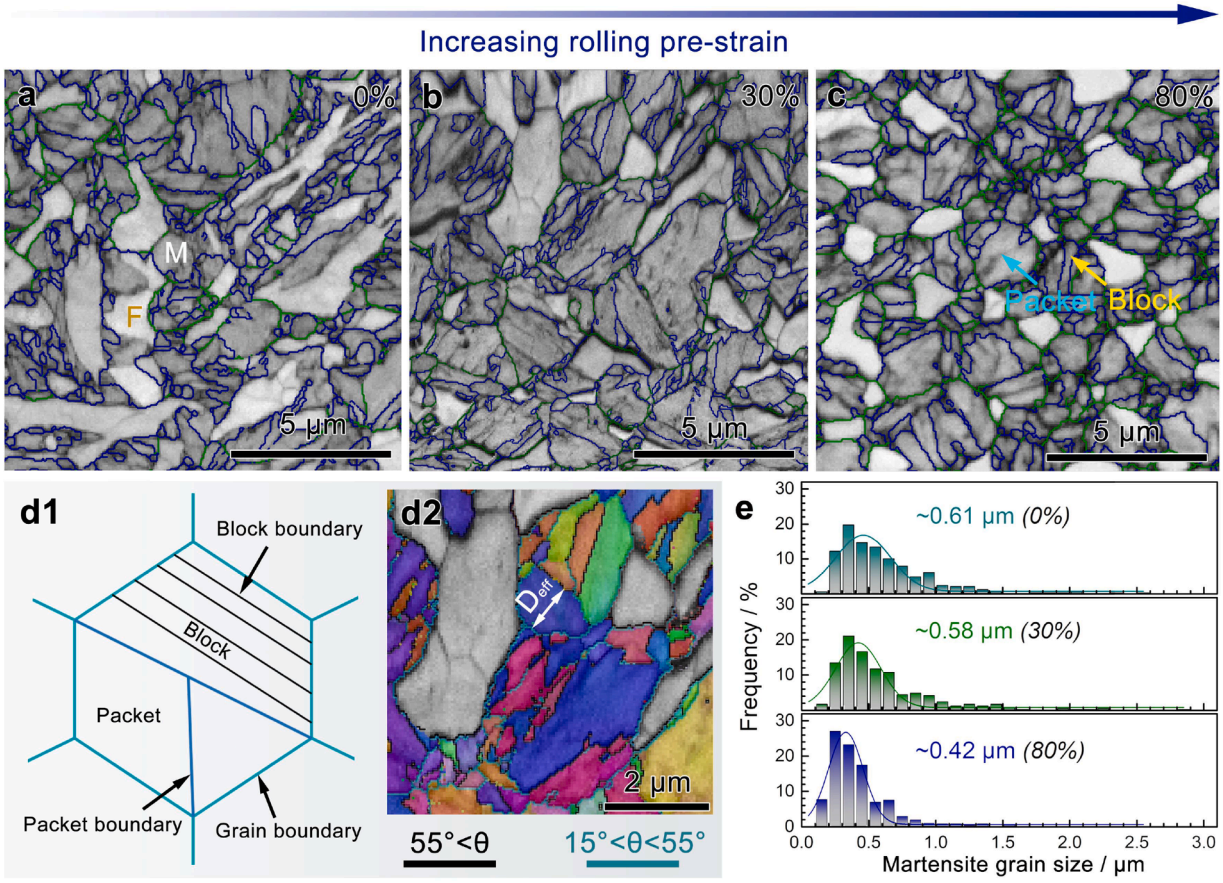

Fig. 3. Effects of initial rolling strain on martensitic structure. (a)–(c) EBSD maps of the rolled steels annealed at 760 °C for 15 min, (d1) schematic showing the hierarchical structure of lath martensite, (d2) IPF map showing the measurement of D_M, (e) distribution of D_M for the rolled steels annealed at 760 °C for 15 min.

As shown in Fig. 4b, the tensile properties of the IA treated DP steels depend strongly on both the initial rolling pre-strain and the annealing duration. Increasing either parameter leads to progressive strengthening, resulting in the ultrahigh UTS of 2.0 GPa achieved in HSDP3 sample. Although the UE decreases with prolonged annealing, the loss is substantially mitigated in the 80% rolled steel (from 8.4% to 5.8%) compared with the 0% and 30% rolled conditions (from 11.9% to 4% and from 9.8% to 5.6%, respectively). This retained ductility, together with the exceptionally high strength, produces a distinctive strength-ductility synergy in HSDP3 steel. Fig. 4c further reveals that HSDP3 sample exhibits a markedly higher strain-hardening rate throughout deformation than the WR80% sample and the lower-strain HSDP steels (HSDP1 and HSDP2). The enhanced strain-hardening capacity delays the onset of necking and is primarily responsible for the improved ductility at such high strength levels. A broader comparison with reported low-carbon steels (Fig. 4d) indicates the exceptional mechanical properties of the present dual-phase heterostructured steels [21,27,31,37,42–48]. Notably, HSDP3 steel achieves an ultra-high strength of 2.0 GPa while maintaining considerable ductility, outperforming conventional low-carbon steels and setting a benchmark for strength-ductility combinations in dual-phase steel systems.

The comparison has also been performed with the reported 2 GPa-grade ultrastrong steels, i.e., martensitic, maraging, TRIP, and Medium Mn steels (Fig. S2). Note that the HSDP3 steel presents a decent strength-ductility combination between the ultrastrong TRIP and Medium Mn steels, meanwhile surpassing the ultrastrong martensitic and maraging steels. As compared to those ultrastrong steels associated with high-alloy contents (e.g., Ni, Co, Mn), the HSDP3 steel achieves its 2 GPa-grade performance within a low-carbon low-alloy framework. This materials plainification strategy offers potential advantages in terms of reduced raw material costs and enhanced weldability [49]. These results demonstrate that the heterostructure design strategy is a potent paradigm for enhancing the competitive advantage of the low-cost alloys by maximizing their intrinsic strength–ductility synergy through microstructural engineering.

3.3. HDI stress and hardening

HDI stress and it associated strain hardening play pivotal roles in achieving simultaneous strengthening and toughening [50–52]. As revealed by Bauschinger-type cyclic LUR tests (Fig. 5a), both the 760DP and HSDP3 steels show noticeable hysteresis loops in the LUR curves, indicating the significant Bauschinger and HDI effects caused by the DP heterostructure [53]. The calculated HDI stress increases with applied strain, with that of HSDP3 steel showing a higher magnitude (Fig. 5b1). The increased HDI stress during tension produces extra strain hardening [54,55], which can be obtained from the HDI stress curve ($\Theta_{HDI} = d\sigma_{HDI}/d\varepsilon$). Both Θ_{HDI} of two steels drop with increasing strain, while the HSDP3 steel shows higher Θ_{HDI} than the 760DP steel at the low-strain stage before 3% (Fig. 5b2). The extra HDI hardening contributes to the enhanced strain hardening rate of the HSDP3 steel. Following the relationship between flow stress, HDI stress, and effective stress ($\sigma_{flow} = \sigma_{HDI} + \sigma_{eff}$) [50,56], the relative contributions of HDI stress and effective stress on strengthening can be evaluated by $\sigma_{HDI}/\sigma_{flow}$ and $\sigma_{eff}/\sigma_{flow}$ ratios, respectively. The $\sigma_{HDI}/\sigma_{flow}$ of 760DP steel keeps about 49% after the strain of 1.5%, whereas that of HSDP3 steel increases from 52% to 55% with strain (Fig. 5c1). Correspondingly, the $\sigma_{eff}/\sigma_{flow}$ of HSDP3 steel is lower than that of 760DP steel during deformation (Fig. 5c2). The magnitudes of σ_{HDI} and σ_{eff} are closely associated with evolution of

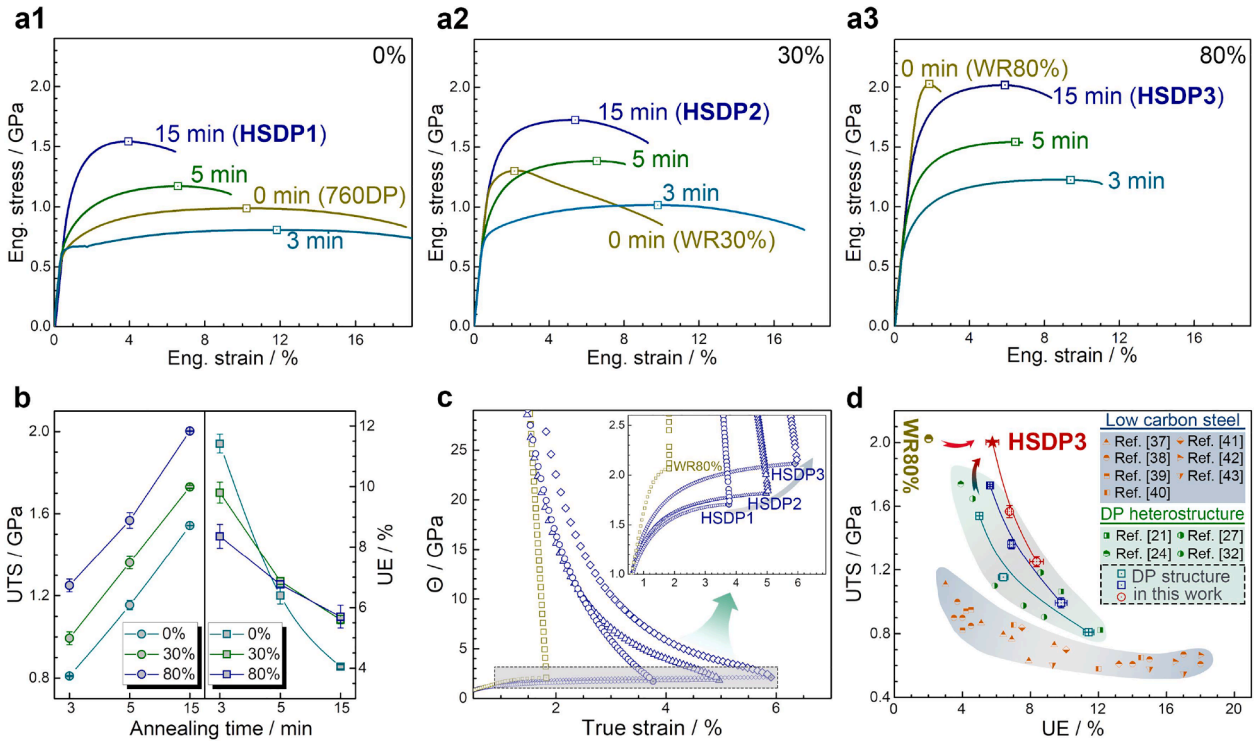

Fig. 4. Mechanical properties of the DP steels. (a1)–(a3) engineering stress-strain curves of DP steels produced from different rolled steels, (b) evolution of UTS and UE with annealing time, (c) true stress and strain hardening rate VS true strain curves for the typical steel samples, (d) comparison of strength-ductility combination of the HSDP3 steel with the low-carbon stees in literatures.

Table 1
Mechanical properties of the steel samples.

samples	IA time	YS (MPa)	UTS (MPa)	UE (%)	ETF (%)
WR0%+760 °C	0 min	643 ± 9	987 ± 11	10.2 ± 0.2	18.6 ± 0.5
	3 min	667 ± 2	808 ± 2	11.9 ± 0.3	25.0 ± 0.7
	5 min	704 ± 10	1138 ± 21	6.0 ± 0.2	9.3 ± 0.8
	15 min	1163 ± 3	1542 ± 1	4.0 ± 0.1	6.4 ± 0.3
WR30%+760 °C	0 min	1192 ± 15	1304 ± 10	2.2 ± 0.4	8.0 ± 2.8
	3 min	750 ± 3	993 ± 31	9.8 ± 0.3	17.5 ± 1.5
	5 min	900 ± 12	1362 ± 30	6.9 ± 0.1	8.0 ± 1.2
	15 min	1292 ± 13	1731 ± 7	5.6 ± 0.1	9.2 ± 0.8
WR80%+760 °C	0 min	1950 ± 11	2021 ± 30	2.1 ± 0.2	2.5 ± 0.1
	3 min	765 ± 8	1250 ± 31	8.4 ± 0.4	10.9 ± 0.2
	5 min	1117 ± 22	1595 ± 38	6.8 ± 0.1	7.0 ± 0.1
	15 min	1544 ± 6	2002 ± 5	5.8 ± 0.4	8.3 ± 0.3

GNDs and statistically stored dislocations (SSDs), which accommodate heterogeneous and homogeneous plastic strain, respectively [57]. Therefore, the proposed dual-phase heterostructure configurations in HSDP3 steel effectively promotes the accumulation of GNDs and providing higher HDI strengthening.

3.4. Synergetic deformation in the dispersed DP heterostructure

3.4.1. Strain and stress evolution during deformation

The superior mechanical properties of HSMs are related to the hetero-zone interactions caused by mechanical incompatibility. To probe the synergetic deformation within heterogeneous zones in the HSDP3 steel with optimized mechanical properties, μ-DIC analysis coupled with SEM imaging across progressive global strains (ε_{global}) were carried out. The normal strain components parallel and perpendicular to the load direction are defined as ε_{xx} and ε_{yy}, respectively. Representative strain maps at the ε_{global}= 1%, 3.5%, and 5.2% are presented in Fig. S3a1-a3 and b1-b3. The ε_{xx} manifests as characteristic tensile strain distribution, while the ε_{yy} dominates by compressive strain. Fig. S3c1-c3 shows the statistical distribution of ε_{xx} at the ε_{global} of 1%, 3.5%, and 5.2%, respectively. The calculated average ε_{xx} are 1.1%, 3.4%, and 5.1%, respectively, consistent with the value of ε_{global}. This verifies the spatial accuracy and resolution of the DIC measurements employed in this study [21]. The typical von Mises equivalent strain (ε_{Mises}) maps superposed on microstructures at different global strains are presented in Fig. 6a1–a3. At initial yielding (ε_{global} = 1%), plastic deformation localizes preferentially in ferrite grains while martensite remains predominantly elastic. Simultaneously, dispersed micro-shear bands (SBs) are nucleated at the hetero boundaries induced by the synergetic deformation of soft and hard zones [17,19]. As plastic deformation progresses to larger strain (ε_{global}: 3.5% and 5.2%), these micro-SBs develop along preferential shear directions orientated at ~45° with respect to the load direction, establishing an intersected network that coordinating plastic flow.

The formation of dispersed micro-SBs is a typical characteristic indicating the deformation heterogeneity in HSMs [14,19,58]. Quantitative strain profiling along the yellow arrow in Fig. 6a3 reveals a heterogeneous strain distribution induced by the micro-SBs (Fig. 6b). The evolution of SBs was evaluated by the height (H) and full width at half maximum (W) extracted from the fitted strain profiles (Fig. 6c). The average H and W at different ε_{global} were calculated based on the statistical analysis of twenty SBs (Fig. 6d). While H increases nearly linearly with ε_{global}, W remains ~2 μm across all macroscopic strain levels. This indicates that, although severe strain localization develops within individual micro-SBs, their dispersed distribution prevents macroscopic

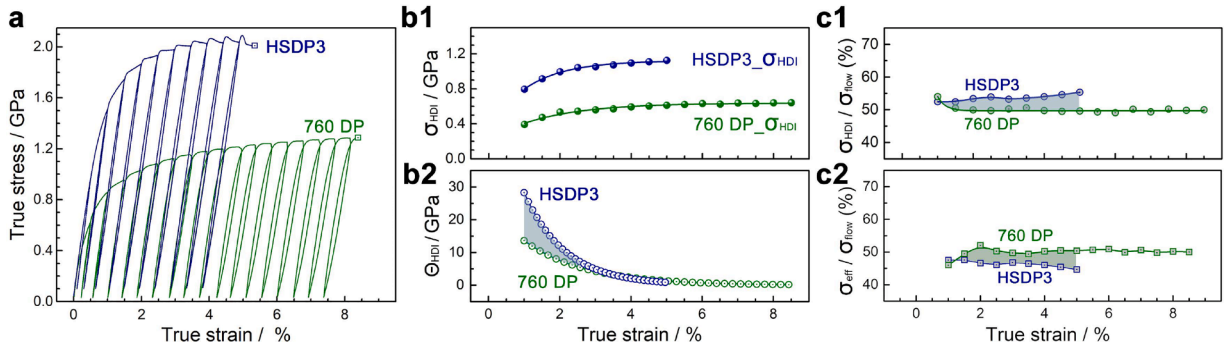

Fig. 5. HDI stress and hardening in the DP steels. (a) LUR true stress-strain curves of 760DP and HSDP3 steels, (b1) and (b2) evolution of σ_{HDI} and Θ_{HDI} with straining, (c1) and (c2) evolution of $\sigma_{HDI}/\sigma_{flow}$ and $\sigma_{eff}/\sigma_{flow}$ during tensile deformation.

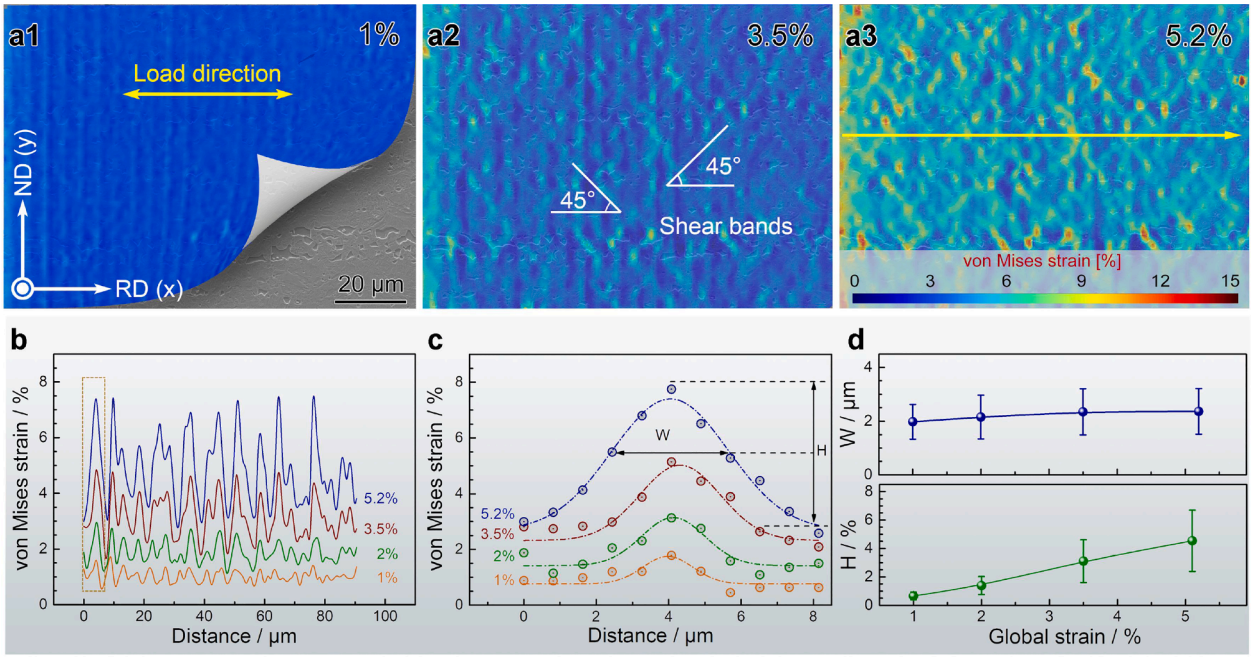

Fig. 6. Evolution of dispersed micro shear bands during tensile deformation. (a1)–(a3) evolution of strain distribution with the ε_{global} of 1%, 3.5% and 5.2%, respectively, (b) strain distribution at different ε_{global} along the yellow arrows in a3, (c) enlarged view of the first strain peak in b to show the H and W obtained from the Gauss fitted strain profile, (d) evolution of average W and H with global strains.

strain localization, thereby enabling stable plastic deformation [14,59].

High-magnification strain mapping at ε_{global} of 5.2% (Fig. 7a1) reveals contrasting deformation behavior between shear-banding and non-shear-banding zones. Within active SBs, both ferrite and martensite undergo substantial plastic strain, while martensite outside these SBs exhibits only minimal deformation. A magnified view of the representative region marked in Fig. 7a2 provides a detailed comparison: the strain distributions extracted along the white and yellow arrows (Fig. 7b1 and b2) show the strain evolution in non-shear-banding and shear-banding zones, respectively. At the ε_{global} of 5.2%, the local strain in ferrite rises up to ~12%, while that of martensite in the non-shear-banding zones keeps low ~2%, resulting in significant strain partitioning with adjacent ferrite. Conversely, martensite inside shear-banding zones undergoes larger plastic strain, attaining ~6% at the same ε_{global}. Therefore, the dispersed SBs network leads to a hierarchical deformation mode in HSDP3 steel, including the deformed ferrite, severely deformed martensite (M_{severe}), and slightly deformed martensite (M_{slight}). Based on the statistical analysis on the strain maps, the strain distributions of ferrite and martensite zones at different ε_{global} are presented in Fig. 7c1 and c2. As ε_{global} increases from 1% to 5.2%, both the average strain in ferrite (ε_F) and martensite (ε_M) increase. Notably, ε_M exhibits a bimodal distribution at the ε_{global} of 3.5% and 5.2%, indicating the strain heterogeneity in martensite induced by the dispersed micro-SBs. Because ε_F increases faster than ε_M, the strain partitioning between the phases ($\varepsilon_F - \varepsilon_M$) grows progressively with deformation (Fig. 7d1). This strain incompatibility also produces a strain gradient ($\omega = d\varepsilon/dx$) across F-M interfaces, quantified following Ref. [20]. The average strain gradient ($\overline{\omega}$) increases with increasing ε_{global} (Fig. 7d2).

DIC results confirm that dispersed SBs emerge as characteristic features of hetero-zone interactions during plastic deformation. To elucidate micro-SBs formation mechanisms and their effect on the deformation behavior of HSDP3 steel, the representative volume element finite elements (RVEFE) simulation was conducted using experimentally characterized microstructures. The details about the finite elements modeling analysis are presented in the supplementary materials. Fig. 8a1-a4 show the evolution of Mises stress at ε_{global} of 1%, 1.5%, 3%, and 5%, respectively, delineating three distinct development stages of micro-SBs: nucleation, propagating, and stabilization. Initial strain application ($\varepsilon_{global} = 1\%$) induces significant stress partitioning in the DP steel, where the stress in martensite is larger than in ferrite. It is

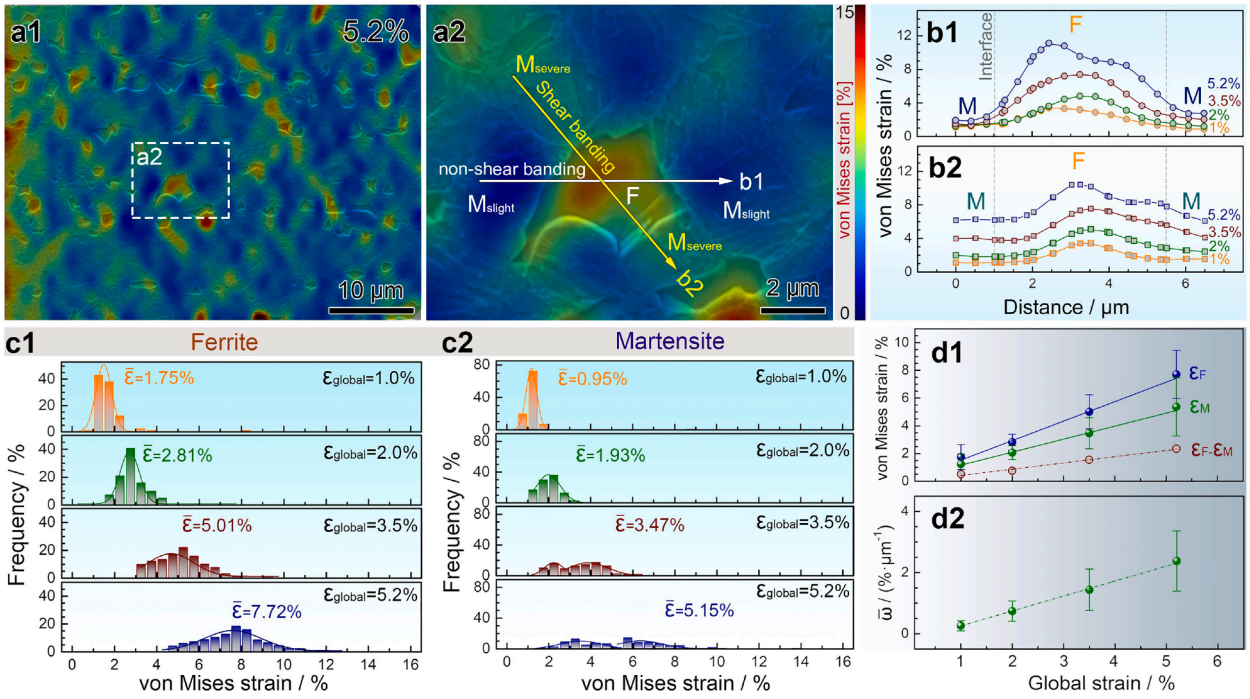

Fig. 7. Effect of micro shear bands on strain distribution in ferrite and martensite. (a1) and (a2) high magnification strain maps of HSDP3 steel at the ε_{global} of 5.2%, (b1) and (b2) strain distribution along the arrows in a2, (c1) and (c2) strain distribution in ferrite and martensite at different ε_{global}, (d1) evolution of average ε_F, ε_M, and $(\varepsilon_F - \varepsilon_M)$ with ε_{global}, (d2) evolution of strain gradient with ε_{global}.

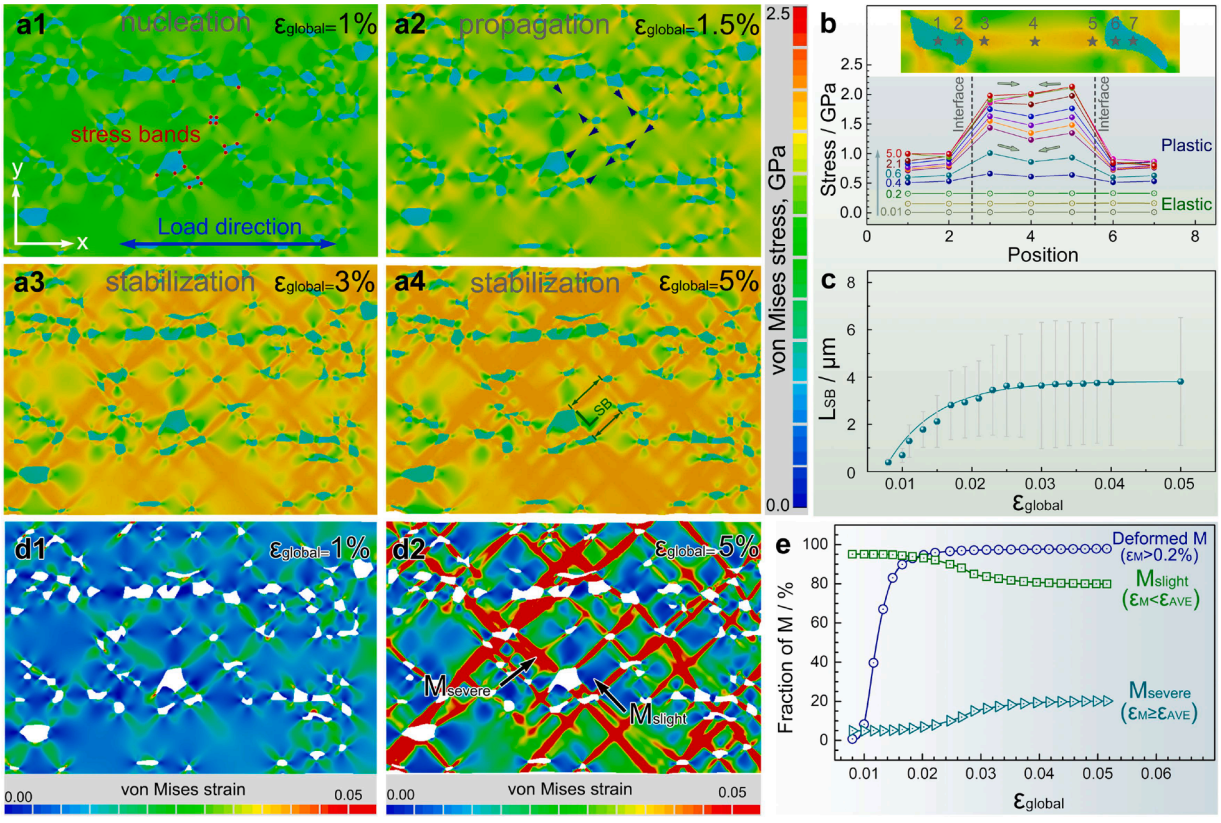

Fig. 8. Stress distribution and evolution of SBs analyzed using RVEFE simulation. (a1)–(a4) distribution of von Mises stress during tensile deformation, (b) evolution of stress along the typical SB at different ε_{global}, (c) evolution of L_{SB} with ε_{global}, (d1) and (d2) strain distribution in martensitic zones at the ε_{global} of 1% and 5%, respectively, (e) fraction of deformed martensite at different ε_{global}.

noted that stress concentrations at F-M interfaces is much larger than those within martensite interiors. This high interfacial stress generates

stress bands orientated the load direction with ~45°, marked by red dots in Fig. 8a1, which serve as preferential SB nucleation sites. With increasing strain, SBs propagate along preferential shear directions, accompanied by local stress transfer from F-M interfaces to the martensite interiors. The oppositely oriented SBs coalesce into extended deformation channels, as pointed by the blue arrows in Fig. 8a2. Typically, the stress evolution along a developed SB is presented in Fig. 8b Initially, interfacial regions (Positions 3 and 5) sustain higher local stress than the martensite interior (Position 4), but upon further deformation (ε_{global} = 2.1%), stress levels along the SB homogenize, indicating the stabilization of deformation in SBs. In addition, the average length of SBs (L_{SB}) increases rapidly at strain below 2% and then saturates at ~3 μm (Fig. 8c), indicating the stabilization of dispersed SBs at large stains.

The evolution of SBs has significant influence on the deformation behavior of the constituent phases, especially the martensitic phase. Fig. 8d1 and d2 show the strain distributions in martensitic zones at ε_{global} of 1% and 5%, respectively, with a 0.2% strain threshold to distinguish deformed and undeformed martensite. Almost 98% of the martensite experiences plastic deformation after ε_{global} of 2% (Fig. 8e). Dispersed micro-SBs result in the notable strain heterogeneity in martensite, partitioning the deformed martensitic zones into two categories: M_{slight} with strain lower than the average strain ($\varepsilon_M < \varepsilon_{AVE}$), and M_{severe} with strain larger than ε_{AVE} ($\varepsilon_M \geq \varepsilon_{AVE}$). The fraction of the M_{slight} decreases with increasing ε_{global}, while that of the M_{severe} increases. Their fractions stabilize at ~80% and ~20%, respectively, after ε_{global} of 3% consistent with the stabilization of micro-SBs.

Both the DIC experiments and RVEFE simulation demonstrate the deformation heterogeneity in martensitic zones around the deformed ferrite. The difference in strain partitioning with the central ferrite therefore occurs due to the difference in carried strain of surrounding martensite. The partitioned strain in martensite (ε_M) is associated with its strength and bearing stress, particularly in conventional DP steels with a lower martensite fraction [60]. Typically, an increase in average martensite grain size results in a higher average equivalent plastic strain within the martensite due to its decreased strength [61]. Based on this consideration, the grain size of M_{severe} should be larger than that of M_{slight}. However, M_{slight} and M_{severe} exhibit almost identical effective grain size (0.38 and 0.39 μm) in the HSDP3 steel, as shown in Fig. S4. In other words, ε_M in the HSDP3 steel is independent of the local grain size and strength of martensite.

In conventional DP steels, martensite is embedded within an interconnected ferrite matrix. Plastic flow propagates in the ferrite, bypassing the high-strength martensitic grains and passing through the low-strength ones [21]. This results in the dependence of ε_M on the grain size and strength of martensite. Conversely, ferrite is fully constrained by the martensitic matrix in the HSDP3 steel, and plastic flow predominantly propagates through the dispersed micro-SBs. The following characteristics of micro-SBs explain the fact that the ε_M is independent of grain size, which consequently leads to identical average grain sizes for M_{slight} and M_{severe}. First, maximum shear stress generally occurs on planes at ~ 45° during uniaxial tension, facilitating preferential plastic flow and propagation of micro-SBs along the maximum shear force direction [11,14]. The stable development of micro-SBs accommodates most of the plastic strain and transfers high stress along shear direction (Fig. 8a3 and a4), causing the martensite grains along the micro-SBs, i.e., oriented at ~ 45° with respect to the ferrite (namely $M_{45°}$) to continuously undergo plastic deformation, regardless of their grain size. This leads to a corresponding lower bearing stress and strain in the martensite approximately parallel and perpendicular to the tensile direction ($M_{0°}$ and $M_{90°}$). As a result, these martensitic grains maintain stronger strain partitioning with the embedded ferrite at elevated ε_{global}. Second, the uniform distribution of micro-SBs enables martensite of various grain sizes to accommodate greater plastic deformation, thereby weakening the conventional dependence of ε_M on martensitic grain size or strength.

3.4.2. Evolution of substructures during tension deformation

Systematic investigations were carried out to reveal dynamic evolution of substructure of ferrite in HSDP3 steel. Interrupted tensile testing combined with EBSD analysis (Fig. 9a1, a2, and b1) demonstrates growth of dislocation density in ferrite, increasing from 1.0 × 10^{15} m^{-2} at a ε_{global} of 3% to 1.4 × 10^{15} m^{-2} at 5%. As shown in Fig. 9b2, the dislocation accumulation leads to an enhancement in local accumulated misorientation (Acc. Mis.) within individual grains along the marked paths (yellow arrows) in Fig. 9a1 and a2, respectively. TEM characterization (Fig. 9c1-c3) further identifies the substructural evolution in the deformed ferrite. In the undeformed state (ε_{global}=0%), high-density dislocations are localized near the F-M interfaces due to the phase transformation during quenching [27], while the dislocation density in the grain interior is lower (Fig. 9c1). With increasing ε_{global} to 3%, dislocations in ferrite accumulate and entangle, resulting in the formation of dislocation cell walls (Fig. 9c2), which preferentially formed near the F-M interfaces because of the initial high-density GNDs nearby [62]. Further deformation to ε_{global} = 5% promotes the sharping of these walls, effectively subdividing ferrite grains into well-defined dislocation cells with size of several hundred micrometers (Fig. 9c3). As a result, the microstructural evolution of ferrite during deformation is associated with the progressive development and refinement of dislocation substructures. For one thing, the average cell size decreases from 1.0 μm to 0.5 μm and 0.3 μm with increasing strain, reflecting enhanced dislocation storage (Fig. 9d). For another, dislocation rearrangement transforms initially thick cell boundaries (~ 100 nm) into sharp and low-energy configurations (~10 nm) (Fig. 9e1 and e2), indicating dynamic recovery at high strains [63]. The resulting dislocation-depleted cell interior is induced by the dislocation trapping at the refined cell walls, further stabilizing the evolved substructures [64,65].

The coordinated deformation between ferrite and martensite within shear-banding zones plays a pivotal role in enhancing deformation compatibility across heterostructures, which is fundamental to the superior mechanical properties of HSDP3 steel. To clarify the deformation response of martensite in these critical regions, the microstructure of the M_{severe} adjacent to the ferrite at a ε_{global} of 5% was investigated using site-specific focused iron beam (FIB) sampling (Fig. 10a1-a3) followed by combined TEM and EBSD characterizations. Compared with undeformed martensite, the fraction of low-angle boundaries (LABs) increases from 22% to 57% (Fig. 10b1 and c1), accompanied by an increase of dislocation density from 1.6 × 10^{15} m^{-2} to 3.3 × 10^{15} m^{-2} (Fig. 10b2 and c2). This value also exceeds the average dislocation density of martensite (M_{Ave}, 2.4 × 10^{15} m^{-2}) at ε_{global} of 5%, contributed by the intensified dislocation activity within SBs. TEM observations of the M_{severe} is shown in Fig. 10d and e. Micro-SBs induce distinct deformation signatures that certain martensite laths become kinked through SB interactions, demonstrating substantial shear strain accommodation. Additionally, localized dissolution of lath boundaries occurs, with these regions evolving into dislocation-dense cell structures. The mechanism of microstructural evolution in M_{severe} is schematically summarized in Fig. 10f. Pre-existing low-angle lath boundaries are progressively modified through shear-induced dislocation accumulation, leading to lath kinking and ultimately to lath boundary disintegration [66]. At advanced deformation stage, the microstructure is dominated by high-density dislocation cells inside the prior martensite blocks. This strain-dependent evolution enables martensite to deform cooperatively with ferrite, thereby maintaining deformation compatibility within micro-SBs.

4. Discussion

4.1. Formation of dispersed DP heterostructure through tuning phase transformation and recrystallization

Increasing warm rolling strain results in a higher V_M and a finer grain

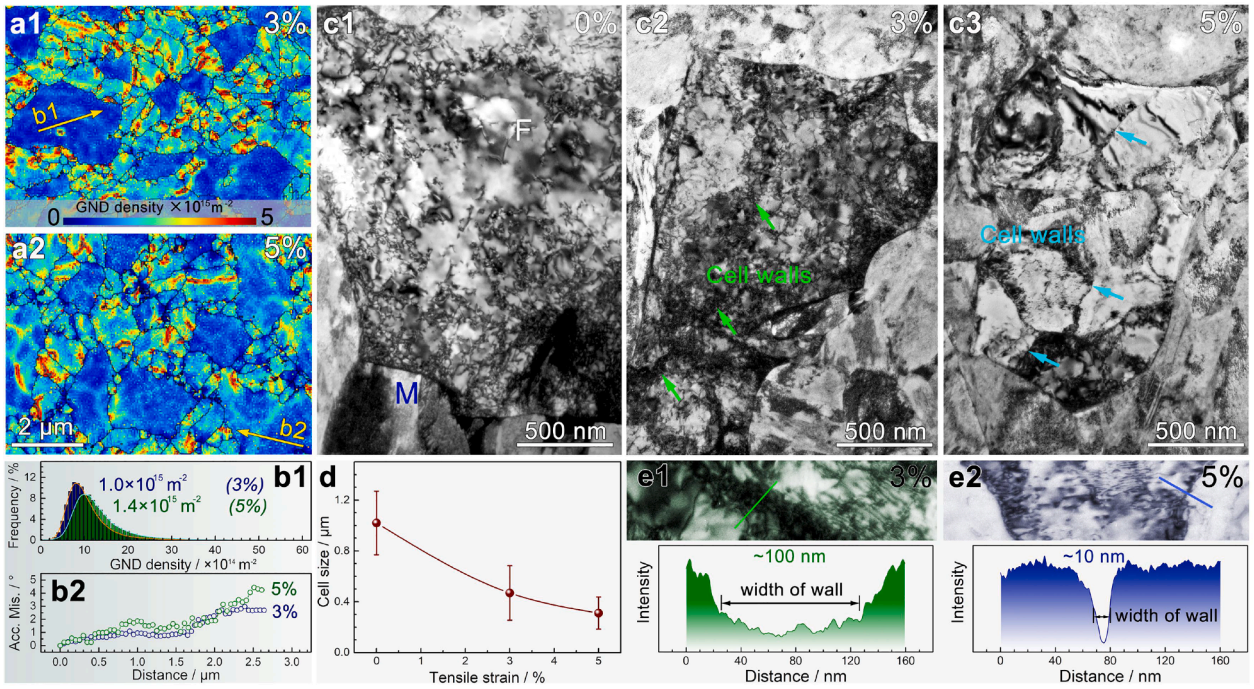

Fig. 9. Evolution of substructures in ferrite during deformation. (a1) and (a2) GND density maps of HSDP3 steel at ε_{global} of 3% and 5%, (b1) GND distribution in the ferrite grains at the strain of 3% and 5%, (b2) accumulative misorientation varying with distance along the yellow arrows in a1 and a2, (c1)–(c3) bright-field TEM micrographs of the HSDP3 steel at ε_{global} of 0%, 3%, and 5%, (d) evolution of average dislocation cell size with tensile strain, (e1) and (e2) measurement of cell wall width at the ε_{global} of 3% and 5%, respectively.

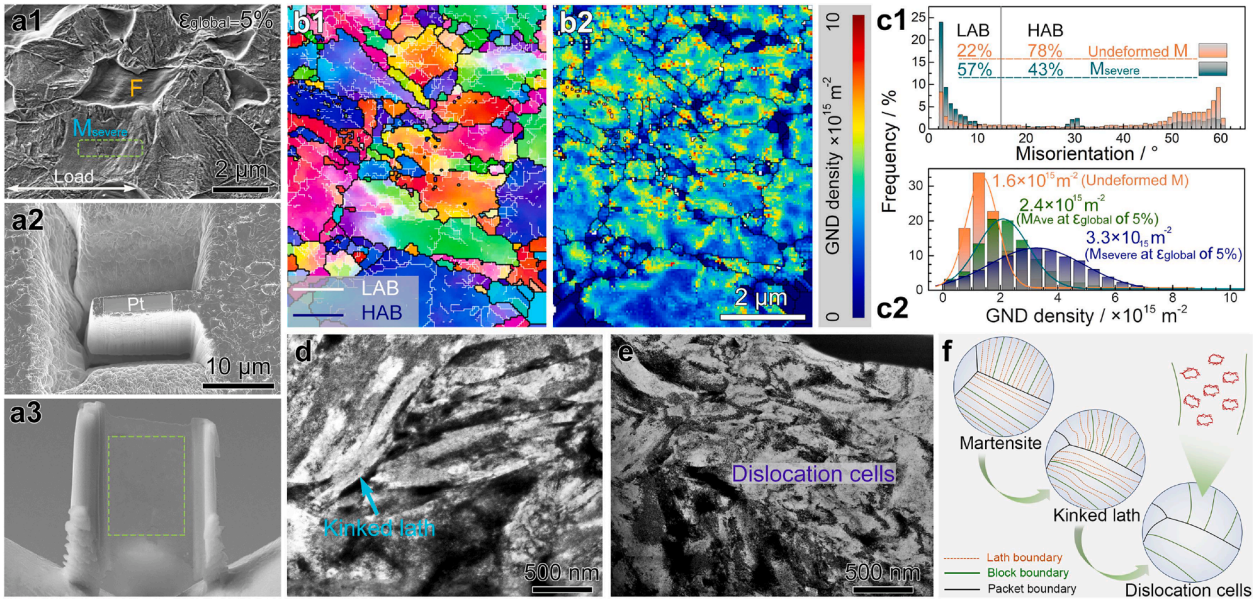

Fig. 10. Deformation response of martensite in the shear-banding zones. (a1) SEM image showing the deformed DP structure at ε_{global} of 5%, (a2) and (a3) lifting the TEM sample of M_{severe} in the shear-banding zone using FIB technique, (b1) and (b2) TKD IPF and GND density maps of the selected region in a3, (c) distribution of misorientation and GND density in M_{severe}, (d) and (e) bright-field TEM micrographs showing the microstructure of M_{severe} in shear-banding zones, (f) schematic illustration showing the substructure evolution of the deformed martensite.

size under identical heat-treatment conditions. This behavior is attributed to both austenite formation and ferrite recrystallization [67,68]. Quantitative analysis through the modified Johnson–Mehl–Avrami–Kolmogorov (JMAK) model reveals fundamental transformation kinetics during intercritical annealing (Eq. (3.1)) [69]:

$$\alpha = V_\gamma / V_e = 1 - \exp\left(-kt^n\right) \tag{3.1}$$

where V_γ and V_e are actual and equilibrium austenite volume fraction, respectively, t is annealing time, n is the JMAK exponent, and k is the temperature-dependent rate constant. It is assumed that all austenite can be transformed into martensite after quenching. Therefore, V_γ is equal to V_M. The logarithmic form of Eq. (3.1) is expressed as:

$$ln\ln(1/1-\alpha) = lnk + nlnt \tag{3.2}$$

The JMAK exponent (n) can be obtained by linear regression from the $lnln(1/(1-\alpha))$ vs $ln(t)$ curve (Fig. S5a). The exponent n is an indicator of the nucleation mode and growth dimensionality. According to different kinetics analysis, in diffusion-controlled growth, the values of n are between 0.5 and 2.5 [69,70]. The calculated exponent n for the DP steels produced from 0%, 30%, and 80% rolling strains are 0.77 to 0.8 and 0.92, respectively, indicating that the similar nucleation and growth mechanism. While the austenite formation is enhanced in the WR80% steel within the same annealing duration. This enhancement originates from strain-induced nano-lamellar structures and dispersed carbides that provide high-density defects and interfaces (Fig. S5f), facilitating carbon diffusion and generating abundant austenite nucleation sites [37]. The resultant refined austenite grains translate to martensitic hierarchical refinement during subsequent quenching [71].

The evolution of DP structure is further affected by competing interactions between austenite formation and ferrite recrystallization [72]. In the 80% rolled steel, ferrite recrystallization precedes austenite formation, as evidenced by fully equiaxed fine grains appearing after 3-min annealing before the completion of austenitization (Fig. S5b and c). This sequence is driven by enhanced strain-stored energy within the nano-lamellar structures, which provides a strong thermodynamic driving force for recrystallization [73]. As a result, significant recrystallization results in the formation of fine equiaxed ferrite grains. In contrast, insufficient grain refinement in the 0% and 30%-rolled steel leads to the incomplete recrystallization with coexistence of recrystallized and elongated fibrous grains (Fig. S5d and e). Moreover, the promoted austenite nucleation in the 80%-rolled steel constrains recrystallized grain growth through interface pinning [74], resulting in the fine ferrite in the dispersed heterostructured DP steel.

4.2. Dispersed micro-SBs and its induced hierarchical plastic deformation

The formation of dispersed micro-SBs is induced by microstructural heterogeneity and the evolution of internal stresses [58,75]. Once yielding, strain incompatibility between phases results in inter-zone constraints that transfer load from ferrite to martensite [76], while GNDs pile-up at F-M interfaces promotes local stress concentrations [77,78]. Once a critical stress is reached, coordinated plastic deformation is activated in martensite. Consequently, SBs preferentially nucleate in martensite near the F-M interfaces (Fig. 8a), where micro plastic instability is readily triggered at sites of elevated distortion energy to alleviate local stress concentration. With increasing strain, these SBs propagate in martensitic zones. DIC results (Fig. 6) reveals that the micro-SBs propagation primarily aligns at approximately 45° to the tension axis, which is consistent with that reported in the laminate Cu/CuZn alloy [11], gradient structured Ni [14], bimodal structured Cu [19], and heterogeneous grain structured Al0.1CoCrFeNi alloy [24]. It seems that the propagation direction is independent of specific heterostructure categories or material systems. It aligns with the direction of maximum shear force, which is realized more easily on shear banding planes ~45° The RVE modeling results (Fig. 8a1-a4) further demonstrate that the equivalent stress at ~45° to the loading axis significantly exceeds that of other orientations, indicating that the propagation path of the micro-SBs is potentially driven by shear stress. Furthermore, grain orientation and spatial distribution have significant influences on the propagation of Micro-SBs. As indicated by the distribution of Schmidt factor (m) in the HSDP3 steel (Fig. S6), both ferrite and martensite grains exhibit a high average Schmidt factor ($\overline{m}$=0.46). This random orientation distribution facilitates activation of dislocation slip in ferrite and martensite to accommodate plastic strain along the shear direction without changing propagation path. In conventional dual-phase steels with interconnected ferrite, micro-SBs tend to propagate rapidly and coalesce into irregular macroscopic strain bands due to the unimpeded stress paths [21]. In contrast, in the HSDP3 steel the fine ferrite is embedded in martensitic matrix. The enhanced inter-zone constraint in this configuration makes it difficult for the stress transfer in neighboring ferrite grains, thereby ensuring a stable propagation path. The UFG martensitic grains does not have enough strain hardening capability to arrest the local shear instability, which permits the propagation of local shear instability along the preferred shear orientation [19]. The propagation of micro-SBs can be dynamically stabilized through interactions with surrounding softer zones. In previous reported heterostructures, such as nanocrystalline-coarse grained Ni [14,58], dual-phase containing deformed iron and recrystallized copper [79], where soft zones with high strain hardening help with decreasing the stress concentration at the SB fronts and suppress unstable propagation. In the present work, as the Micro-SBs propagate to approach the F-M interfaces, the high local stress will be relieved by the boosted dislocation activity in the ferrite grains with superior strain hardening ability and favorable Schmidt factor [18,22,58]. In addition, dispersed distribution of heterogeneous zones produces denser hetero boundaries, as verified by the constitutive modeling [20]. This confines the free propagation path to limit the propagation of micro-SBs. These characteristics of ferritic zones are conductive to stabilize the micro-SBs.

The ferritic zones therefore play a key role in both the nucleation and stabilization of SBs in the hierarchical plastic deformation. The grain size and distribution of ferrite have significant influences on micro-SBs characteristics and mechanical properties. To investigate this effect, statistically similar representative volume element (SSRVE) models with assumed dimensional size of 60 × 40 μm were constructed (Fig. 11). Specifically, four models with a same ferrite volume fraction ($V_F = 18\%$) but varying ferrite grain sizes (1.02 to 2.88 μm) were examined (Fig. 11a1-a4). Grain refinement changes the ferrite distribution from clustered to dispersed, resulting in a corresponding transition from localized to uniformly distributed SBs (Fig. 11b1-b4). Fig. 11c reveals a linear decrease in SB density with increasing ferrite grain size. In the sample with clustered ferrite, penetrative shear bands form at ε_{global} of 4% (Fig. 11b1), leading to catastrophic shear instability. In contrast, the dispersed DP heterostructure provides higher-density F-M interfaces for dispersed nucleation of micro-SBs [20]. The dispersed DP structure also impedes SBs propagation through geometric constraint imposed by finely distributed ferrite grains. This stabilizes micro-SBs within martensitic zones, thus preventing catastrophic shear localization.

The dispersed micro-SBs modify deformation behavior and mechanical properties of the DP steel through constructing a hierarchical plastic deformation within dual-phase heterostructure. The heterogeneous plastic deformation in DP structure is primarily manifested as the strain partitioning between ferrite and martensite, which has been widely reported in previous studies [21,80]. In the present study, it is found that during the co-deformation stage of ferrite and martensite, the plastic strain in martensite shows a bimodal distribution (Fig. 7c2), induced by the high-density of intersecting micro-SBs. Therefore, martensite deformation proceeds via two distinct strain accommodation modes: M_{slight} in the non-shear banding zones and M_{severe} within SBs. The M_{slight}regions, which account for approximatel 80% of martensite throughout deformation (Fig. 8e), exhibit limited strain compatibility with adjacent ferrite, thereby intensifying strain partitioning and promoting the development of HDI stress. Concurrently, the M_{severe} zones enable localized high-strain accommodation without catastrophic failure.

Generally, the emergence of macroscopic shear bands in metallic materials triggers the severe strain localization, leading to premature shear instability and failure [81]. In the current HSDP3 steel, however, the micro-SBs is stabilized through the mechanical constraint of surrounding soft zones. Importantly, the dispersed stable micro-SBs enhances inter-zone deformation compatibility to improve strain hardening and mechanical properties. First, the formation of dispersed micro-SBs enables a larger volume fraction of the martensitic matrix to participate in strain accommodation, particularly at high global strain levels. As the ferritic grains become finer and dispersed, the fraction of M_{severe} increases (Fig. 11d), accompanied by improved strain hardening

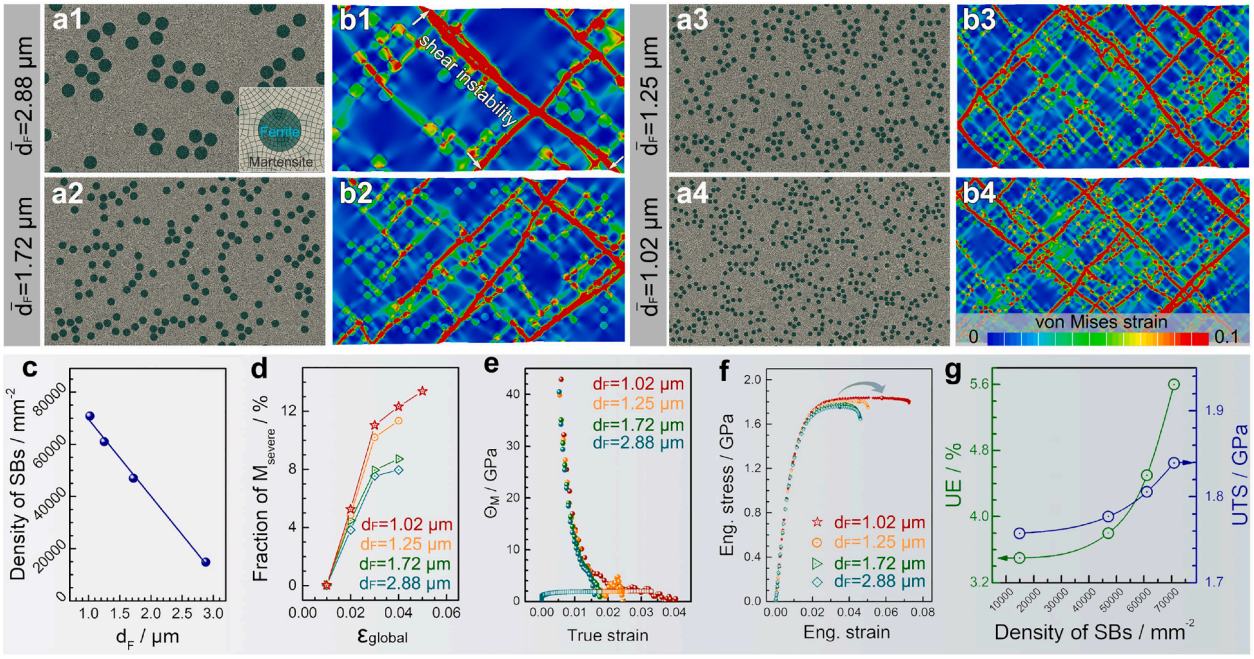

Fig. 11. SSRVE simulation to investigate the effect of ferrite grain size and distribution on the evolution of SBs. (a1)–(a4) the SSRVE models for the DP steels with the same ferrite content but different ferrite grain sizes, (b1)–(b4) corresponding von Mises strain maps of DP steels at the ε_{global} of 4%, (c) relationship between ferrite grain size and density of SBs, (d) varying fraction of M_{severe} with ε_{global}, (e) calculated strain hardening rate curves of martensite in the DP steels with different ferritic characteristics, (f) the calculated engineering stress-strain curves of the DP steels with different ferritic grain sizes, (g) evolution of UE and UTS with SBs density.

capacity and ductility within the martensite itself (Fig. 11e). This is conductive to the enhancement in total strain hardening and mitigation

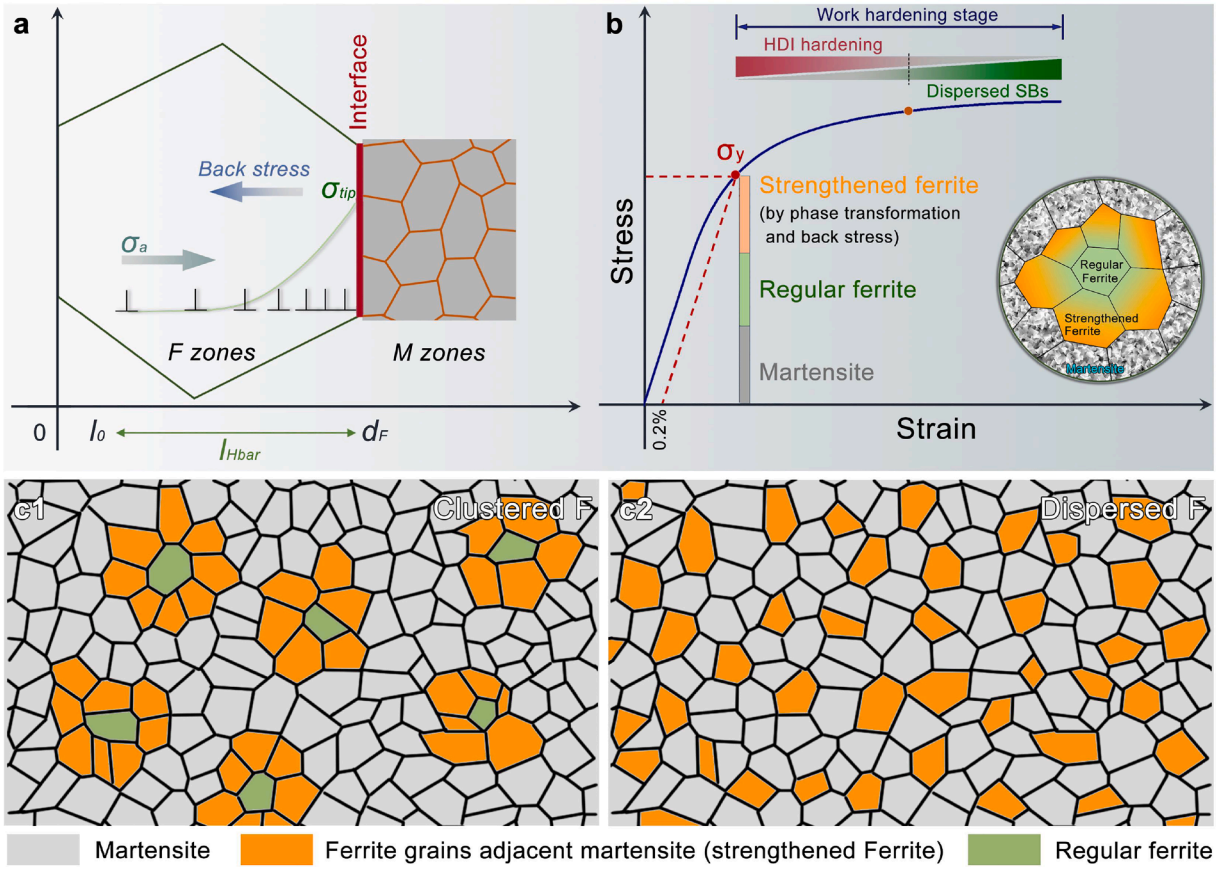

Fig. 12. Schematical illustration of the strengthening and ductilization mechanisms of HSDP3 steel. (a) the Hbar and tip stress, (b) illustrate showing the contributors to the strength and ductility of HSDP3 steel, (c1) and (c2) two different distributions of ferrite grains in steels.

of localized plastic instability [82,83]. Second, the propagation of micro-SBs facilitates effective stress transfer from the hard martensite to the softer ferrite, thus promoting dislocation accumulation in soft zones to enhance strain hardening. As verified in the calculated engineering stress-strain curves of different modeling samples (Fig. 11f), both of the tensile strength and ductility increase with formation of denser micro-SBs (Fig. 11g).

4.3. Strengthening and toughening through inter-zone synergetic effects

Generally, the yield strength of DP steels can be estimated using the mixture law [84]:

$$\sigma_y = \sigma_F V_F + \sigma_M V_M \tag{4}$$

where σ_F and σ_M represent the yield stress of ferrite and martensite calculated from the flow stress curves of Fig. S7 in the supplementary materials. The calculated yield strength through the mixture rule is only 1365 MPa, which is lower than the experimental results of HSDP3 steel (1543 MPa). This discrepancy reveals critical contributions from HDI stress, particularly back stress strengthening at the yield point [85]. Chou's enhanced model quantifies this effect through Eq. (5) [86]:

$$\sigma_y = \sigma_M V_M + \sigma_{F,\,b}\ V_{b,\,F} + \sigma_F\left(V_F - V_{F,\,b}\right) \tag{5}$$

where $\sigma_{F,b}$ is the yield stress of the ferrite grains against martensite, $V_{F,\,b}$ is the fraction of the ferrite grains adjacent to martensite. The accumulation of back stress is related to the hetero boundary affected regions (Hbar) and the GND density (N_{Hbar}) in the Hbar [11,20,87]. The Hbar in DP steel is the region near the F-M interface induced by GNDs pileups, and the effective length of dislocation pileups is equal to the width of Hbar (l_{Hbar}) (Fig. 12a). The relationship between l_{Hbar} and N_{Hbar} can be expressed as [86]:

$$l_{Hbar} = \left[1 - \left(\frac{\sigma_F}{\sigma_M}\right)^2\right] d_F \tag{6.1}$$

$$N_{Hbar} = \frac{2\pi(1-\nu)k d_M^{-1/2}}{M\mu(2-\nu)b} l_{Hbar} \tag{6.2}$$

where d_F and d_M are the effective grain size of ferrite and martensite, ν, M, μ, and b are the Poisson ratio, Taylor constant, shear modulus, and magnitude of Burgers vector, respectively. The effective pileups in Hbar results in a gradient distribution of back stress, and the stress at the tip of the pile up (σ_{tip}) can be written as:

$$\sigma_{tip} = N_{Hbar}(\sigma_a - \sigma_0) = \frac{2\pi(1-\nu)k^2 d_F}{M\mu(2-\nu)b d_M}\left[1 - \left(\frac{\sigma_F}{\sigma_M}\right)^2\right] \tag{6.3}$$

where k is a Hall-Petch constant, σ_a is the applied shear stress, σ_0 is the friction stress of ~50 MPa [88]. This local stress σ_{tip}, several times higher than applied stress (σ_a), impedes further movement of leading dislocations across the hetero boundaries. $\sigma_{F,b}$ is then expressed as:

$$\sigma_{F,b} = \sigma_0 + \sqrt{\frac{M\mu(2-\nu)b\sigma_{tip}}{\pi(1-\nu)d_F} + \sigma_F^2} \tag{6.4}$$

The $\sigma_{F,b}$ in the HSDP3 steel is calculated as 1116 MPa, a value below the yield stress of surrounding martensitic phases. In fact, the ferritic characteristics has great influences on the local yield behavior. In DP steels, ferrite grains are situated either adjacent to martensite or neighboring other ferrite grains. The austenite-to-martensite phase transformation during quenching involves a volume expansion, resulting in the formation of plastically deformed zone in the ferrite adjacent to martensite and residual stress near F-M interfaces. This phase transformation induces higher density of pre-existing dislocations and substantial long-range internal stress in the ferrite near martensite compared to the ferrite-ferrite regions. These pre-existing features before tension deformation primarily result in the low elastic limit and continuous yielding [28]. Additionally, as the soft ferrite is surrounded by the hard martensite, it restricts the ferrite from changing the shape as required during plastic deformation until the hard martensite starts to deform plastically. Therefore, high-density GNDs pile up at the zone boundaries to accommodate heterogeneous plastic strain, resulting in the buildup of high back stress inside the ferrite grains. These facts collectively make the soft ferrite surrounded by martensite become stronger than that free of martensitic constraint. Consequently, σ_y here is contributed by the martensite, regular ferrite, and the strengthened ferrite (Fig. 12b). In the HSDP3 steel, almost every ferritic grain is embedded in martensite (Fig. 2c3). Therefore, $V_{F,\,b}$ is equal to V_F, meaning that all of the ferritic grains can be strengthened by back stress during deformation.

The modified mixture rule (Eq. (5)) predicts an overall σ_y of 1492 MPa for DP steel, closely matching experimental measurements. This correlation confirms that microstructural optimization significantly influences back stress strengthening effect. As schematically shown in Fig. 12c1 and c2, the dispersed dual-phase heterostructure can effectively increase the $V_{F,\,b}$ (the orange ferrite grains) as compared to the clustered ones under the same fraction of ferrite grains, maximizing back stress strengthening in soft zones to achieve higher strength. This microstructural design strategy transforms soft ferrite into a secondary strengthening source alongside martensite, surpassing traditional mixture rule predictions.

The inter-zone synergetic effects, particularly HDI hardening and dispersed SBs, in the HSDP3 steel critically enhance strain hardening and ductility. The kinetic HDI strain hardening arises from the progressive increase of HDI stress with applied strain governed by GND accumulations [12,89]. The total HDI stress is proportional to the gradient of GND density [90]. Given the proportional relationship between GND density (ρ_{GND}) and strain gradient (ω), $\rho_{GND} = K|\omega|/b$ [91], HDI stress should theoretically increase linearly with strain gradient. In the present study, the average strain gradient in the HSDP3 steel increases linearly with global strain (Fig. 7d2), but the HDI stress does not increase linearly with strain gradient. The fast increase of HDI stress at the low-strain stage is attributed to the quick GND accumulations during the elastic-plastic transition stage, while the slowdown is probably induced by the dynamic disappearance of dislocations in ferritic grains. High-density dislocation cells are formed in ferrite during deformation (Fig. 9c2 and c3). The dislocation traps near dislocation cells and dynamic recovery result in a counterbalanced storage of glide dislocations [92]. The disappeared GNDs took away their contribution to HDI stress but left strain in their slipping path.

Therefore, HDI hardening dominates strengthening and hardening via rapid accumulation of GNDs during low-strain stage. As strain progresses, mechanical stability becomes primarily sustained by dispersed micro-SBs (Fig. 12b). It is suggested that the strength is closely related to deformation incompatibility near hetero-interfaces, while ductility mainly depends on the coordinated plastic deformation between heterostructures [93,94]. In conventional DP steels with low martensite content (20%−30%), plastic flow bypasses the embedded martensite, while the martensite cannot effectively accommodate plastic strain together with ferrite [21]. This leads to significant strain localization in ferrite and limited strain coordination of martensite, making F-M interfaces easy to be failure. In this work, the promoted plastic deformation in hard martensite, induced by the high-density stable micro-SBs, is realized by deploying higher volume fraction of hard zones and dispersed soft zones. This strategy significantly prevents strain localization and sustains ductility at high stress level. The performance of the hard zones proves critical in this configuration for comprehensively implementing inter-zone synergetic effects. The hierarchical fine structure of lath martensite in the HSDP3 steel, characterized by high-density high-angle grain boundaries, provides dual mechanical advantages through boundary strengthening and fracture toughness enhancement

via crack deflection mechanisms [39]. This strength-toughness balance allows martensitic zones to fulfill complementary roles of effective constrainer at low strains and plastic accommodator at high strains, thus better realizing the inter-zone synergetic effects.

5. Conclusions

To sum up, this work clarifies how heterogeneous zones configuration and inter-zone synergetic effects on the mechanical properties of a dual-phase heterostructure. By rationally tailoring the spatial distribution of soft and hard zones, strength and ductility are simultaneously enhanced through micro-shear-band-mediated inter-zone interactions. The effects of dual-phase configurations on micro-shear-band formation and their effects on deformation behaviors of heterogenous zones were systematically investigated. The key findings are summarized as follows.

(1) Controlled rolling pre-strain followed by annealing enables precise regulation of phase fraction, spatial distribution, and grain size. Increasing rolling pre-strain refines the grain size from 404 to 181 and ultimately to 28 nm, promoting the formation of fine-grained dual-phase structures. Extended annealing time further modifies ferrite grain size and distribution via an increased martensite volume fraction (V_M). A large rolling pre-strain (80% reduction, $\varepsilon = 1.86$) combined with prolonged annealing (15 min) produces a dispersed heterostructured dual-phase steel (HSDP3), in which equiaxed ferrite (~1 μm) is uniformly embedded within an ultrafine-grained martensitic matrix (V_M: 82%).

(2) Dispersed micro-SBs represent a typical deformation feature of HSDP3 steel, evolving through nucleation, propagation, and stabilization. Micro-SBs preferentially nucleate at ferrite–martensite interfaces and propagate along favored shear directions under long-range internal stresses. Equiaxed ferritic zones with high strain-hardening capacity effectively impede micro-SB propagation. The refined and dispersed ferrite in HSDP3 generates a high density of interfaces, promoting the formation of dense and stable micro-SBs.

(3) The micro-SBs induce a hierarchical deformation mode comprising deformed ferrite, severely deformed martensite (M_{severe}), and slightly deformed martensite (M_{slight}). After a global strain of 3%, volume fractions of M_{severe} and M_{slight} stabilize at ~20% and ~80%, respectively. Ferrite accommodates strain through dynamic refinement of dislocation cell structures, whereas M_{slight} outside shear bands undertake minimal strain, enabling effective strain partitioning and the development of hetero-deformation-induced stress. In contrast, martensite within shear bands accommodates higher strain via kinked laths and dense dislocation substructures.

(4) HSDP3 steel achieves an ultrahigh strength of 2.0 GPa while retaining considerable ductility, with a markedly enhanced strain-hardening rate compared to the as-rolled and lower-strain HSDP steels. This superior strength–ductility synergy results from the optimized heterostructure and micro-shear-band-mediated inter-zone interactions. Confining ferritic grains within the martensitic matrix leads to effective back-stress strengthening, while dense, stable micro-SBs suppress catastrophic shear localization and enhance strain hardening, synergistically improving strength and ductility.

CRediT authorship contribution statement

Bo Gao: Writing – review & editing, Writing – original draft, Methodology, Investigation, Funding acquisition, Data curation. **Xinxin Dong:** Validation, Investigation, Funding acquisition, Formal analysis. **Lirong Xiao:** Validation, Methodology, Conceptualization. **Yi Liu:** Validation, Methodology. **Dongdi Yin:** Writing – review & editing, Formal analysis, Conceptualization. **Hao Zhou:** Writing – review & editing, Supervision, Investigation, Funding acquisition, Data curation, Conceptualization. **Yuntian Zhu:** Supervision, Funding acquisition, Conceptualization.

Declaration of interests

The authors declare that they have no known competing financial interests or personal relationships that could have appeared to influence the work reported in this paper.

Acknowledgements

This work was supported by the National Key R&D Program of China (grant number 2021YFA1200203), the National Natural Science Foundation of China (grant numbers 52201124, 52571139, 52401153), the Natural Science Foundation of Jiangsu Province (grant number BK20220960).

Supplementary materials

Supplementary material associated with this article can be found, in the online version, at doi:10.1016/j.actamat.2026.122232.

References

[1] J. Zhao, Z. Jiang, Thermomechanical processing of advanced high strength steels, Prog. Mater. Sci. 94 (2018) 174–242.
[2] C. Hu, X. Wan, Y. Zhang, R. Ke, T. Furuhara, Making ultra-high-yield-strength and high-ductility austenitic stainless steel by grain refinement and regularly arranging Cu-nanoprecipitates, Mater. Res. Lett. 13 (2025) 1091–1098.
[3] X. Li, L. Chen, Y. Zhao, R.D.K. Misra, Influence of manganese content on ε-/α′-martensitic transformation and tensile properties of low-C high-Mn TRIP steels, Mater. Des. 142 (2018) 190–202.
[4] J.H. Choi, M.C. Jo, H. Lee, A. Zargaran, T. Song, S.S. Sohn, N.J. Kim, S. Lee, Cu addition effects on TRIP to TWIP transition and tensile property improvement of ultra-high-strength austenitic high-Mn steels, Acta Mater. 166 (2019) 246–260.
[5] J. Hou, L. Jing, B. Cao, Y. Zhao, Z. Ren, T. Wang, Z. Wang, H.S. Kim, T. Yang, Heterostructure-enabled creep resistance and deformation mechanisms in a new Ni-Co-based high-entropy alloy, Mater. Res. Lett. 13 (2025) 1242–1251.
[6] S.Y. Tung, Y.C. Chen, Y. Zhu, M.H. Tsai, Achieving ideal hetero-lamella structure for superior strength–ductility in a medium-entropy alloy via engineering initial grain size, Acta Mater. 302 (2026) 121675.
[7] Y. Yu, Z. Guan, J. Chen, J. Song, P. Ma, Substantial enhancement of strength and corrosion resistance in magnesium alloy via a multi-component gradient heterostructure, Mater. Res. Lett. 13 (2025) 1125–1132.
[8] Q. Cheng, B. Yang, C. Zhang, X. Chen, W. Su, X. Lu, J. Liang, W. Cao, C. Huang, Optimizing strength-ductility synergy in lightweight steel via heterogeneous design: discontinuous fibrous ferrite, Mater. Res. Lett. 12 (2024) 947–955.
[9] X. Wu, M. Yang, F. Yuan, G. Wu, Y. Wei, X. Huang, Y. Zhu, Heterogeneous lamella structure unites ultrafine-grain strength with coarse-grain ductility, Proc. Natl. Acad. Sci. U. S. A. 112 (47) (2015) 14501–14505.
[10] H. Yang, G. Wang, M. Zhu, J. Guo, N. Chen, H. Kou, Tailoring hierarchical deformation mechanisms in metastable β titanium alloy via heterogeneous lamellar β structure design, Mater. Res. Lett. 13 (2025) 1053–1061.
[11] C.X. Huang, Y.F. Wang, X.L. Ma, S. Yin, H.W. Höppel, M. Göken, X.L. Wu, H.J. Gao, Y.T. Zhu, Interface affected zone for optimal strength and ductility in heterogeneous laminate, Mater. Today 21 (2018) 713–719.
[12] X. Ma, C. Huang, J. Moering, M. Ruppert, H.W. Höppel, M. Göken, J. Narayan, Y. Zhu, Mechanical properties of copper/bronze laminates: role of interfaces, Acta Mater. 116 (2016) 43–52.
[13] G. Li, J. Jiang, H. Ma, R. Zheng, S. Gao, S. Zhao, C. Ma, K. Ameyama, B. Ding, X. Li, Superior strength–ductility synergy in three-dimensional heterogeneous-nanostructured metals, Acta Mater. 256 (2023) 119143.
[14] Y. Wang, C. Huang, Y. Li, F. Guo, Q. He, M. Wang, X. Wu, R.O. Scattergood, Y. Zhu, Dense dispersed shear bands in gradient-structured Ni, Int. J. Plast. 124 (2020) 186–198.
[15] B. Gao, X. Dong, X. Chen, L. Xiao, Q. Zhou, X. Han, D. Yin, H. Zhou, Y. Zhu, Heterostructure enables new deformation mechanisms to enhance strength and work hardening, Mater. Res. Lett. 13 (9) (2025) 917–927.
[16] H. Zhou, X. Wu, D. Srolovitz, Y. Zhu, Designing heterostructured materials, Nature Mater. 25 (3) (2026) 366–372.
[17] Y. Wang, Y. Wei, Z. Zhao, Z. Lin, F. Guo, Q. Cheng, C. Huang, Y. Zhu, Mechanical response of the constrained nanostructured layer in heterogeneous laminate, Scripta Mater. 207 (2022) 114310.

[18] Y. Wang, Y. Wei, Z. Zhao, H. Long, Z. Lin, F. Guo, Q. He, C. Huang, Y. Zhu, Activating dispersed strain bands in tensioned nanostructure layer for high ductility: the effects of microstructure inhomogeneity, Int. J. Plast. 149 (2022).
[19] Y.F. Wang, C.X. Huang, Q. He, F.J. Guo, M.S. Wang, L.Y. Song, Y.T. Zhu, Heterostructure induced dispersive shear bands in heterostructured Cu, Scripta Mater. 170 (2019) 76–80.
[20] Y. Wang, Y. Zhu, Z. Yu, J. Zhao, Y. Wei, Hetero-zone boundary affected region: a primary microstructural factor controlling extra work hardening in heterostructure, Acta Mater. 241 (2022) 118395.
[21] B. Gao, Y. Liu, X. Chen, Y. Sui, W. Sun, L. Xiao, H. Zhou, Heterogeneous plastic deformation and HDI strengthening of the heterostructured dual-phase steels investigated by in-situ SEM-DIC, Mater. Sci. Eng. A 893 (2024) 146149.
[22] B. Gao, L. Wang, Y. Liu, J. Liu, L. Xiao, Y. Sui, W. Sun, X. Chen, H. Zhou, Enhanced strength and ductility of the low-carbon steel with heterogeneous lamellar dual-phase structure produced by cyclic intercritical rolling, J. Mater. Res. Technol. 23 (2023) 6230–6243.
[23] Y. Wang, X. Ma, F. Guo, Z. Zhao, C. Huang, Y. Zhu, Y. Wei, Strong and ductile CrCoNi medium-entropy alloy via dispersed heterostructure, Mater. Des. 225 (2023) 111593.
[24] J. Li, X. Ma, K. Lu, Y. Wang, Y. Zhu, Unusual deformation mechanisms evoked by hetero-zone interaction in a heterostructured FCC high-entropy alloy, Acta Mater. 282 (2025) 120516.
[25] K. Lu, X. Ma, Y. Zhu, Prolonged martensitic transformation induced by heterogeneous deformation in a heterostructured metastable high-entropy alloy, Scripta Mater. 269 (2025) 116912.
[26] T. Liu, X. Zhang, W. Song, C. Li, P. Wang, D. Li, Y. Zhu, Y. Li, Dynamic hetero-deformation induced hardening through strength reversal between hetero-zones in austenite-ferrite duplex steel, Acta Mater. 293 (2025) 121120.
[27] B. Gao, X. Chen, Z. Pan, J. Li, Y. Ma, Y. Cao, M. Liu, Q. Lai, L. Xiao, H. Zhou, A high-strength heterogeneous structural dual-phase steel, J. Mater. Sci. 54 (2019) 12898–12910.
[28] M. Calcagnotto, Y. Adachi, D. Ponge, D. Raabe, Deformation and fracture mechanisms in fine- and ultrafine-grained ferrite/martensite dual-phase steels and the effect of aging, Acta Mater. 59 (2011) 658–670.
[29] N. Peranio, Y.J. Li, F. Roters, D. Raabe, Microstructure and texture evolution in dual-phase steels: competition between recovery, recrystallization, and phase transformation, Mater. Sci. Eng. A 527 (2010) 4161–4168.
[30] Q. Lai, H. Yang, Y. Wei, H. Zhou, L. Xiao, H. Ying, S. Lan, Z. You, Z. Kou, T. Feng, Q. Lu, P. Jacques, T. Pardoen, Transformation plasticity in high strength, ductile ultrafine-grained FeMn alloy processed by heavy ausforming, Int. J. Plast. 148 (2022) 103151.
[31] J.X. Huang, Y. Liu, T. Xu, X.F. Chen, Q.Q. Lai, L.R. Xiao, Z.Y. Pan, B. Gao, H. Zhou, Y.T. Zhu, Dual-phase hetero-structured strategy to improve ductility of a low carbon martensitic steel, Materi. Sci. Eng. A 834 (2022) 142584.
[32] Q. Lai, L. Brassart, O. Bouaziz, M. Gouné, M. Verdier, G. Parry, A. Perlade, Y. Bréchet, T. Pardoen, Influence of martensite volume fraction and hardness on the plastic behavior of dual-phase steels: experiments and micromechanical modeling, Int. J. Plast. 80 (2016) 187–203.
[33] A. Tang, H. Liu, G. Liu, Y. Zhong, L. Wang, Q. Lu, J. Wang, Y. Shen, Lognormal distribution of local strain: a universal law of plastic deformation in material, Phys. Rev. Lett. 124 (15) (2020) 155501.
[34] A. Tang, H. Liu, R. Chen, G. Liu, Q. Lai, Y. Zhong, L. Wang, J. Wang, Q. Lu, Y. Shen, Mesoscopic origin of damage nucleation in dual-phase steels, Int. J. Plast. 137 (2021) 102920.
[35] N. Kamikawa, M. Hirohashi, Y. Sato, E. Chandiran, G. Miyamoto, T. Furuhara, Tensile behavior of ferrite-martensite dual phase steels with nano-precipitation of vanadium carbides, ISIJ Inter. 55 (8) (2015) 1781–1790.
[36] B. Gao, Q. Lai, Y. Cao, R. Hu, L. Xiao, Z. Pan, N. Liang, Y. Li, G. Sha, M. Liu, H. Zhou, X. Wu, Y. Zhu, Ultrastrong low-carbon nanosteel produced by heterostructure and interstitial mediated warm rolling, Sci. Adv. 6 (39) (2020) eaba8169.
[37] B. Gao, R. Hu, Z. Pan, X. Chen, Y. Liu, L. Xiao, Y. Cao, Y. Li, Q. Lai, H. Zhou, Strengthening and ductilization of laminate dual-phase steels with high martensite content, J. Mater. Sci. Technol. 65 (2021) 29–37.
[38] T. Karthikeyan, M.K. Dash, S. Saroja, M. Vijayalakshmi, Estimation of martensite feature size in a low-carbon alloy steel by microtexture analysis of boundaries, Micron 68 (2015) 77–90.
[39] B. Gao, L. Wang, Y. Liu, J. Liu, L. Xiao, Y. Sui, W. Sun, X. Chen, H. Zhou, Achieving ultrahigh strength by tuning the hierarchical structure of low-carbon martensitic steel, Mater. Sci. Eng. A 881 (2023) 145370.
[40] Y. Wang, J. Sun, T. Jiang, Y. Sun, S. Guo, Y. Liu, A low-alloy high-carbon martensite steel with 2.6 GPa tensile strength and good ductility, Acta Mater. 158 (2018) 247–256.
[41] H. Luo, X. Wang, Z. Liu, Z. Yang, Influence of refined hierarchical martensitic microstructures on yield strength and impact toughness of ultra-high strength stainless steel, J. Mater. Sci. Technol. 51 (2020) 130–136.
[42] E. Ahmad, T. Manzoor, N. Hussain, Thermomechanical processing in the intercritical region and tensile properties of dual-phase steel, Mater. Sci. Eng. A 508 (1) (2009) 259–265.
[43] M. Balbi, I. Alvarez-Armas, A. Armas, Effect of holding time at an intercritical temperature on the microstructure and tensile properties of a ferrite-martensite dual phase steel, Mater. Sci. Eng. A 733 (2018) 1–8.
[44] S. Li, G. Zhu, Y. Kang, Effect of substructure on mechanical properties and fracture behavior of lath martensite in 0.1C-1.1Si-1.7Mn steel, J. Alloys Compd. 675 (2016) 104–115.
[45] A. Karmakar, A. Karani, S. Patra, D. Chakrabarti, Development of bimodal ferrite-grain structures in low-carbon steel using rapid intercritical annealing, Metall. Mater. Trans. A 44 (5) (2013) 2041–2052.
[46] Y.G. Deng, H.S. Di, J.C. Zhang, Effect of heat-treatment schedule on the microstructure and mechanical properties of cold-rolled dual-phase steels, Acta Metall. Sinica (English Letters) 28 (9) (2015) 1141–1148.
[47] Q. Meng, J. Li, H. Zheng, High-efficiency fast-heating annealing of a cold-rolled dual-phase steel, Mater. Des. 58 (2014) 194–197.
[48] M. Soleimani, H. Mirzadeh, C. Dehghanian, Effects of tempering on the mechanical and corrosion properties of dual phase steel, Mater. Today Commun. 22 (2020) 100745.
[49] X. Li, K. Lu, Improving sustainability with simpler alloys, Science 364 (2019) 733–734.
[50] Y. Zhu, X. Wu, Heterostructured materials, Prog. Mater. Sci. 131 (2023) 101019.
[51] G.H. Gu, Y. Kim, H.S. Kim, Back stress quantification in heterostructured metals: a comparative study of tension-compression and loading-unloading-reloading tests, Mater. Res. Lett. 13 (2025) 1189–1198.
[52] R. Zhong, W. Zhang, C. Zhao, Z. Luo, H. Dong, Achieving an ultrastrong yet ductile copper alloy via microstructural heterogeneity with dense ordered nanoprecipitates, Mater. Res. Lett. 13 (2025) 875–884.
[53] C. Guo, H. Liu, F. Chen, R. Ma, B. Cong, H. Zhang, J. Zou, X. Liu, H. Nagaumi, Achieving strength-ductility synergy in novel heterogeneous lamella structures of Al-Mg-*Sc*-Zr-Ag alloys, Mater. Res. Lett. 13 (2025) 392–400.
[54] X.T. Fang, G.Z. He, C. Zheng, X.L. Ma, D. Kaoumi, Y.S. Li, Y.T. Zhu, Effect of heterostructure and hetero-deformation induced hardening on the strength and ductility of brass, Acta Mater. 186 (2020) 644–655.
[55] F.J. Guo, Y.F. Wang, M.S. Wang, Q. He, H. Ran, C.X. Huang, Y.T. Zhu, Hetero-deformation induced strengthening and toughening of pure iron with inverse and multi-gradient structures, Mater. Sci. Eng. A 782 (2020) 139256.
[56] R. Chen, G. Liu, P. Wu, Y. Zhang, X. Wang, Y. Shen, Hetero-deformation induced (HDI) stress measurement from the plastic dissipation in the hysteresis loops, Mater. Res. Lett. 13 (3) (2025) 248–255.
[57] N. Wang, Y. Chen, G. Wu, Q. Zhao, Z. Zhang, L. Zhu, J. Luo, Non-equivalence contribution of geometrically necessary dislocation and statistically stored dislocation in work-hardened metals, Mater. Sci. Eng. A 836 (2022) 142728.
[58] Y. Wang, C. Huang, Z. Li, X. Fang, M. Wang, Q. He, F. Guo, Y. Zhu, Shear band stability and uniform elongation of gradient structured material: role of lateral constraint, Extreme Mech. Lett. 37 (2020) 100686.
[59] S. Wei, J. Kim, C.C. Tasan, In-situ investigation of plasticity in a Ti-Al-V-Fe (α+β) alloy: slip mechanisms, strain localization, and partitioning, Int. J. Plast. 148 (2022) 103131.
[60] M.H. Park, Y. Fujimura, A. Shibata, N. Tsuji, Effect of martensite hardness on mechanical properties and stress/strain-partitioning behavior in ferrite + martensite dual-phase steels, Mater. Sci. Eng. A 916 (2024) 147301.
[61] P. Dastur, C. Slater, T. Moore, C. Davis, Martensite size and morphology influence on strain distribution and micro-damage evolution in dual-phase steels; comparing segregation-neutralised and banded grades, Mater. Des. 246 (2024) 113340.
[62] D.A. Korzekwa, D.K. Matlock, G. Krauss, Dislocation substructure as a function of strain in a dual-phase steel, Metall. Trans. A 15 (1984) 1221–1228.
[63] U.F. Kocks, T. Hasegawa, R.O. Scattergood, On the origin of cell walls and of lattice misorientations during deformation, Scripta Metall. 14 (1980) 449–454.
[64] K.S. Ng, A.H.W. Ngan, Effects of trapping dislocations within small crystals on their deformation behavior, Acta Mater. 57 (2009) 4902–4910.
[65] P. Hähner, A theory of dislocation cell formation based on stochastic dislocation dynamics, Acta Mater. 44 (1996) 2345–2352.
[66] S. Morito, T. Ohba, A.K. Das, T. Hayashi, M. Yoshida, Effect of solution carbon and retained austenite films on the development of deformation structures of low-carbon lath martensite, ISIJ Inter. 53 (2013) 2226–2232.
[67] M. Kulakov, W.J. Poole, M. Militzer, The effect of the initial microstructure on recrystallization and austenite formation in a DP600 steel, Metall. Mater. Trans. A 44 (2013) 3564–3576.
[68] D. Barbier, L. Germain, A. Hazotte, M. Gouné, A. Chbihi, Microstructures resulting from the interaction between ferrite recrystallization and austenite formation in dual-phase steels, J. Mater. Sci. 50 (2015) 374–381.
[69] Y. Mazaheri, A. Kermanpur, A. Najafizadeh, A.G. Kalashami, Kinetics of ferrite recrystallization and austenite formation during intercritical annealing of the cold-rolled ferrite/martensite duplex structures, Metall. Mater. Trans. A 47 (2016) 1040–1051.
[70] E. López-Martínez, O. Vázquez-Gómez, H.J. Vergara-Hernández, B. Campillo, Effect of initial microstructure on austenite formation kinetics in high-strength experimental microalloyed steels, Int. J. Minerals, Metallurgy, Mater. 22 (2015) 1304–1312.
[71] S. Kumar, N.N. Pai, S. Manda, U. Tewary, D.T. Fullwood, S.K. Giri, S. Kundu, S.V.S. N. Murty, C.R. Anoop, I. Samajdar, Austenite residual stress and lath martensite variant selection in low carbon steels, Acta Mater. 289 (2025) 120885.
[72] C. Zheng, D. Raabe, Interaction between recrystallization and phase transformation during intercritical annealing in a cold-rolled dual-phase steel: a cellular automaton model, Acta Mater. 61 (2013) 5504–5517.
[73] C. Philippot, M. Bellavoine, M. Dumont, K. Hoummada, J. Drillet, V. Hebert, P. Maugis, Influence of heating rate on ferrite recrystallization and austenite formation in cold-rolled microalloyed dual-phase steels, Metall. Mater. Trans. A 49 (2018) 66–77.
[74] N. Nakada, Y. Arakawa, K.-S. Park, T. Tsuchiyama, S. Takaki, Dual phase structure formed by partial reversion of cold-deformed martensite, Mater. Sci. Eng. A 553 (2012) 128–133.

[75] H. Ma, Y. Zhao, Z. Lyu, X. Wang, Y. Zhu, Y. Gao, What are the "dispersive shear bands" on the surfaces of layered heterostructured materials, J. Mech. Phys. Solids 181 (2023) 105467.
[76] J. Le, Y. Han, M. Fang, S. Li, G. Huang, J. Mao, C.J. Boehlert, W. Lu, A universal shear-lag model for accurate assessment of whisker load-transfer strengthening in metal matrix composites, Comp. Part B: Eng. 247 (2022) 110317.
[77] Y. Xia, T. Yu, Y. Zhang, K. Miao, C.-Y. Chiang, D. Juul Jensen, G. Fan, Activation of unexpected slip systems in the interface affected zone in multilayered aluminum, Mater. Res. Lett. 13 (2025) 963–972.
[78] Y. Zhu, X. Wu, Identifying heterostructured materials, Mater. Res. Lett. 14 (2026) 233–239.
[79] Z. Li, Y. Liu, Y. Wang, J. Hu, L. Xu, J. Wang, C. Liu, Y. Zhu, Hierarchical strain band formation and mechanical behavior of a heterostructured dual-phase material, J. Mater. Sci. Technol. 162 (2023) 25–37.
[80] C. Pelligra, J. Samei, J. Kang, D.S. Wilkinson, The effect of vanadium on microstrain partitioning and localized damage during deformation of unnotched and notched DP1300 steels, Int. J. Plast. 158 (2022) 103435.
[81] M. Gaspérini, C. Pinna, W. Swiatnicki, Microstructure evolution and strain localization during shear deformation of an aluminium alloy, Acta Mater. 44 (10) (1996) 4195–4208.
[82] F. Liang, B. Zhang, Y. Yong, X.M. Luo, G.P. Zhang, Enhanced strain delocalization through formation of dispersive micro shear bands in laminated Ni, Int. J. Plast. 132 (2020) 102745.
[83] W. Qiang, Q. Wu, L. Long, Potential regulation of strength-ductility by nucleation and growth mechanisms of shear bands in heterogeneous laminates, Mater. Today Commun. 38 (2024) 107960.
[84] J. Lian, Z. Jiang, J. Liu, Theoretical model for the tensile work hardening behaviour of dual-phase steel, Mater. Sci. Eng. A 147 (1991) 55–65.
[85] X. Wu, Y. Zhu, Heterogeneous materials: a new class of materials with unprecedented mechanical properties, Mater. Res. Lett. 5 (2017) 527–532.
[86] T.H. Chou, W.P. Li, H.W. Chang, X.H. Du, W.S. Chuang, T. Yang, Y.T. Zhu, J. C. Huang, Quantitative analysis of hetero-deformation induced strengthening in heterogeneous grain structure, Int. J. Plast. 159 (2022) 103482.
[87] Y. Gu, Z. Li, H. Gao, Hetero-boundary-affected regions in heterostructured materials, JOM 75 (2023) 1405–1422.
[88] T. Ohashi, M. Kawamukai, H. Zbib, A multiscale approach for modeling scale-dependent yield stress in polycrystalline metals, Int. J. Plast. 23 (2007) 897–914.
[89] J. Li, G.J. Weng, S. Chen, X. Wu, On strain hardening mechanism in gradient nanostructures, Int. J. Plast. 88 (2017) 89–107.
[90] C.J. Bayley, W.A.M. Brekelmans, M.G.D. Geers, A comparison of dislocation induced back stress formulations in strain gradient crystal plasticity, Int. J. Solids and Struct. 43 (2006) 7268–7286.
[91] H. Gao, Y. Huang, W.D. Nix, J.W. Hutchinson, Mechanism-based strain gradient plasticity— I. Theory, J. Mech. Phys. Solids 47 (1999) 1239–1263.
[92] N. Wang, Y. Chen, G. Wu, Z. Zhang, Z. Wu, J. Luo, Investigation on micro mechanism involved in ferrite hardening after prestraining of dual-phase steel, Mater. Sci. Eng. A 800 (2021) 140387.
[93] F. An, S. Zou, J. Liu, B. Zhang, X. Huang, J. Hou, B. Qian, X. Zhang, W. Lu, Designing ultrahigh-strength lightweight compositionally complex alloys through heterostructural composite engineering, Acta Mater. 297 (2025) 121375.
[94] M.H. Park, A. Shibata, S. Harjo, N. Tsuji, Grain refinement of dual phase steel maximizes deformation ability of martensite, leading to simultaneous enhancement of strength and ductility, Acta Mater. 292 (2025) 121061.